Biophysical*Journal*
Article

Biophysical Society

Enhanced Dynamics of Confined Cytoskeletal Filaments Driven by Asymmetric Motors

Arvind Ravichandran,[1] Gerrit A. Vliegenthart,[1] Guglielmo Saggiorato,[1,2] Thorsten Auth,[1,*] and Gerhard Gompper[1]
[1]Theoretical Soft Matter and Biophysics, Institute of Complex Systems and Institute for Advanced Simulation, Forschungszentrum Jülich, Jülich, Germany and [2]LPTMS, CNRS, University Paris-Sud, Université Paris-Saclay, Orsay, France

ABSTRACT Cytoskeletal filaments and molecular motors facilitate the micron-scale force generation necessary for the distribution of organelles and the restructuring of the cytoskeleton within eukaryotic cells. Although the mesoscopic structure and the dynamics of such filaments have been studied in vitro and in vivo, their connection with filament polarity-dependent motor-mediated force generation is not well understood. Using 2D Brownian dynamics simulations, we study a dense, confined mixture of rigid microtubules (MTs) and active springs that have arms that cross-link neighboring MT pairs and move unidirectionally on the attached MT. We simulate depletion interactions between MTs using an attractive potential. We show that dimeric motors, with a motile arm on only one of the two MTs, produce large polarity-sorted MT clusters, whereas tetrameric motors, with motile arms on both microtubules, produce bundles. Furthermore, dimeric motors induce, on average, higher velocities between antialigned MTs than tetrameric motors. Our results, where MTs move faster near the confining wall, are consistent with experimental observations in *Drosophila* oocytes where enhanced microtubule activity is found close to the confining plasma membrane.

INTRODUCTION

Cytoskeletons of eukaryotic cells contain rigid, polar, filamentous proteins called "microtubules" (MTs). Molecular motors, such as kinesins and dyneins, have arms that cross-link two neighboring MTs, consume energy in the form of ATP, and move toward only one (either plus or minus) end of the attached MT. It has been shown, both in vitro and in vivo, that the motor-arm motion causes the motors to stretch and impart active stresses resulting in MT sliding (1–3). These biological machines connect chemical reactions to mechanical processes in an environment that is out of equilibrium (4). The consequence of such a mechanism is particularly apparent in the case of cytoplasmic streaming. In this process, MT advection causes the cytoplasm to be circulated (5–8). In the *Drosophila* oocyte at midoogenesis, cytosolic molecules, such as the body plan determinant *oskar* mRNA, are localized inhomogeneously within the cell (9). Moreover, the bulk motion of the cytoplasm, driven by kinesin-1 motors, has been shown to drive important processes, such as cell shape change, organelle transport, and nervous system development in *Drosophila* (10,11).

Remarkable examples of these microscopic engines have also been observed in cases of reconstituted systems of MTs and kinesin motors in vitro, e.g., the self-organization of MT–motor protein mixtures into dynamic asters and vortices (12), and the spontaneous motion in an active gel of stabilized MT bundles under the activity of multimotor clusters of kinesins (13,14). When MTs and motors were constrained to the surface of a giant lipid vesicles, spatiotemporal patterns that gave interacting defect configurations and filopodia-like protrusions were observed (15).

Because all of these systems are active and therefore not in thermodynamic equilibrium, they are inherently elusive to classical statistical mechanics (16). This has necessitated new theoretical and numerical approaches in the study of flows and stresses in bulk cytoskeletal networks (17–26). One of the biggest challenges faced in this endeavor is the range of length scales in which dynamics takes place. Capturing the dynamics of individual nanoscopic kinesin motors and microscopic MTs within the same simulation is difficult. Therefore, coarse-grained modeling becomes increasingly important to elucidate generic features and emergent behavior (27), such as the collective effect of individual kinesin motor molecules on MT bundles: each motor entity represents kinesins localized in a region of the MT contour, inducing concerted inter-MT sliding.

Submitted February 27, 2017, and accepted for publication July 27, 2017.

*Correspondence: t.auth@fz-juelich.de

Editor: Alexander Dunn.
http://dx.doi.org/10.1016/j.bpj.2017.07.016

We consider two different types of motors, both of which have been shown in experiments to cross-link and cause relative sliding between MTs. Dimeric motors, e.g., kinesin-1 and kinesin-14 (2,10,28,29), are composed of a motor domain, motile on one MT, and a secondary, nonmotor, MT-binding site that is anchored and not motile on the other MT. Tetrameric motors (e.g., kinesin-5 (30–32)) have two motile motor domains at opposite ends, on both cross-linked MTs. When multiple dimeric motors cross-link a MT pair, tangential forces on the MTs arise based on whether the bound motors are correlated (with all anchored arms on one MT and all motile arms on the other MT) or uncorrelated (with anchored arms and motile arms bound on different MTs). Although many simulations have studied the role of tetrameric motors on MTs (19,21,23,26), important aspects in MT-motor-protein mixtures such as different motor-arm speeds (33), and dimeric motors (34,35), have rarely been considered so far.

Even though cytoskeletal activity inside living cells takes place under the strong effect of confinement of the plasma membrane, only recently have studies addressed its importance in affecting dynamics of active systems (36–38) and intracellular organization. It has been shown that confinement can decrease critical filament density for the isotropic-nematic phase transition (39) and induce formation of clustering and bundlelike structures (40). Also, it is known that confining the cytoskeleton within cells influences mitotic organization and spindle positioning (41,42), the deformation and orientation of the nucleus (43), and cellular protrusions produced by actively treadmilling actin filaments called the “lamellipodium” (44). Inhomogeneities in MT distribution within oocytes have also been reported to be key for bulk motion within the cytoplasm, i.e., a layer of stable, immobile MTs at the oocyte cortex, upon which cytoplasmic MTs push against with the aid of kinesins, was observed (5), further highlighting the importance of confinement.

In coarse-graining the molecular details of the cytoskeleton, most simulation studies have largely ignored attractive interactions between MTs, which can occur from the cytoplasm being a crowded environment (45), where macromolecules occupy 20–30% of the total volume (46). MT bundling frees up additional volume for smaller particles, increasing the overall system entropy, resulting in an effective attraction (47). On top of having an effect on the overall structure of a passive MT system without motors, these cohesive interactions bring MTs together, making them amenable for the cross-linking of molecular motors.

This article is organized as follows. In Methods, the model of a 2D active gel, confined within a circular external boundary, is explained. In Results, the results and analysis of the simulations are described. In particular, in Global Structure, macroscopic structures formed by MTs within the entire confinement are discussed. In Local Polar Order, a local polar order parameter is used to distinguish populations of polar-aligned and antialigned MTs. In Motor-Mediated Motion, MT pair orientation is linked to MT velocity, and the difference between cooperative and antagonistic effects of dimeric motors is distinguished. In Dynamics Near Confinement, the large-scale dynamics of MTs and how they move within the confinement is detailed. In Motor Evolution, lifecycles of the different types of motors and the evolution of their lengths after cross-linking are shown. In Discussion, the connection between our work to existing experimental and theoretical studies is discussed.

METHODS

To study the collective effects of motors on a network of confined MTs, we reduce molecular level details to a 2D coarse-grained model. MTs are described by their center-of-mass, $\boldsymbol{r}_i$, and orientation, $\boldsymbol{p}_i$ (Fig. 1). They are modeled as semipenetrable, rigid rods of length L, discretized into nb beads of diameter $r_{\min}$. We define the bead diameter to be the position of the minimum of the MT-MT interaction potential. In each simulation, we consider a constant number of MTs, N_f, and attached motors, N_m. Motors are modeled as harmonic springs with equilibrium length zero, with two arms, each attached to a point on an MT.

Filaments

Beads of neighboring MTs interact with the separation-shifted Lennard-Jones-like potential (48),

$$U(r) = \begin{cases} \dfrac{A_R}{\left(r^2+\alpha^2\right)^8} - \dfrac{A_A}{\left(r^2+\alpha^2\right)^4} & r \leq 3r_{\min} \\ 0 & r > 3r_{\min} \end{cases}, \quad (1)$$

where r is the distance between two beads belonging to two neighboring MTs; and A_R, A_A, and α determine the energy of the repulsive peak (E_R), the attractive well (E_A), and the position of the energy minimum ($r_{\min}$). This relationship is given in the Supporting Material. In units of thermal energy ($k_B T$), $E_R = 20$ and E_A is varied between 0.2 and 1.0. The aspect ratio of MTs is given by $L/r_{\min} = 5$.

The exponents of the potential are chosen such that the superposition of multiple, overlapping beads gives a smooth, attractive MT-MT interaction, with a repulsive core. At the same time, when the MTs encounter large forces and torques, the capped potential will allow for MTs to slide over each other, resembling a crossing in the third dimension (49,50). The energies associated with the crossing and sliding of MT pairs is discussed in detail in the Supporting Material. To define MT area fraction, we use the length r_{eff}, which is defined by the first peak of the pair correlation function (Fig. S21).

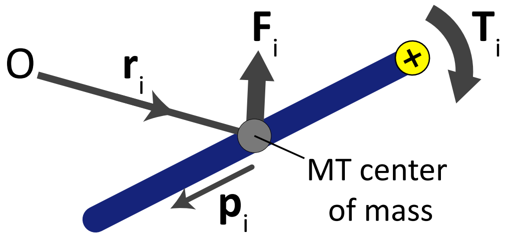

FIGURE 1 Force, $\boldsymbol{F}_i$, and torque, $\boldsymbol{T}_i$, acting on MT i, with center-of-mass, $\boldsymbol{r}_i$, with respect to an origin, O, and orientation, $\boldsymbol{p}_i$, which is in the opposite direction of motor-arm motion. To see this figure in color, go online.

The beads that make up the MTs interact with an attractive, hard, circular wall of radius $R_W/L = 8$, via a Lennard-Jones potential given in Eq. S8 in the Supporting Material. A comparison of MT-wall interactions with other interactions involved in the system is given in the Supporting Material.

Motors

The density of motors on cross-linked MTs depends on MT pairs' overlap lengths, motor speed, and motor concentration in the solution (51). Each motor has two arms that cross-link a MT pair. Dimeric motors have one motile arm and an immobile anchored arm (29). Tetrameric motors have two motile arms that both move toward the positive end of their respective MT, i.e., in the direction $-\boldsymbol{p}_i$ on the MT (Fig. 1).

Because tetrameric motors are symmetric upon motor-arm exchange, only the relative alignment of the cross-linked MTs determines the dynamics (Fig. 2, *A* and *B*). When polar-aligned MTs are cross-linked by tetrameric motors (Fig. 2 *A*), the relative velocities of the MTs are small and the force generated by the molecular motors vanishes. Antialigned MTs cross-linked by tetrameric motors (Fig. 2 *B*), on the other hand, generate the largest tangential velocity between cross-linked MTs because both arms move at the same time.

Dimeric motors are not symmetric with respect to motor-arm exchange. Thus, for two dimeric motors cross-linking two MTs, four states corresponding to two relative combinations of motors, and two combinations of MT polarity (Fig. 2, *C*–*F*), can be constructed. One possibility is that motors bind to MTs in a spatially correlated manner, such that all motors have their motile arms on one MT and the anchored arms on the other MT (Fig. 2, *C* and *D*). In this case, both polar-aligned and antialigned MT orientations cause relative sliding between them. The other possibility is that motors bind in an uncorrelated manner, such that the motile and anchored arms are bound randomly on either MT. Uncorrelated motors cross-linking a polar-aligned MT pair will act antagonistically because the force imparted by a dimeric motor is counteracted by the force imparted by a motor that binds in the conjugate orientation (Fig. 2 *E*). This leads to relatively small forces between MT pairs. Uncorrelated motors between antialigned MTs, however, act cooperatively, and cause relative sliding between MTs (Fig. 2 *F*).

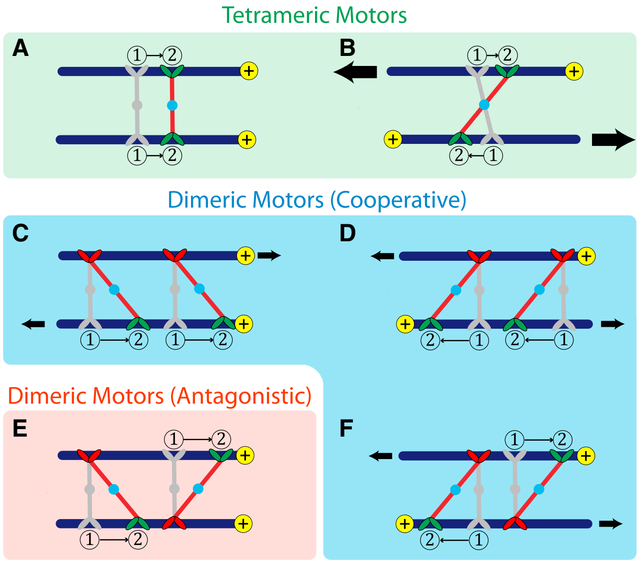

FIGURE 2 Schematic showing the effects of tetrameric and dimeric motors on polar-aligned and antialigned MTs. Motor arms are shown to move from position (1) to position (2), in the direction of MT polarization, represented by the yellow marking at the MT tip. The gray representations show the initial attachment positions of motors. Active motor-arms that move on the MT direction of polarization are colored green, and immobile, anchored motor-arms are colored red. Tetrameric motors have two motile arms on either cross-linking MT. Dimeric motors have an anchored arm and a motile arm. (*A*) Tetrameric motors cross-linking aligned MTs induce small velocities. (*B*) Tetrameric motors cross-linking antialigned MTs induce larger velocities. (*C*) Correlated dimeric motors cross-linking aligned MTs have the same effect as (*D*) dimeric motors cross-linking antialigned MTs. (*E*) Uncorrelated dimeric motors cross-linking aligned MTs act antagonistically, (*F*) whereas uncorrelated dimeric motors cross-linking antialigned MTs act cooperatively. To see this figure in color, go online.

In most cases, MT pairs remain in the polar-aligned (antialigned) orientation for the duration that the motor is bound. This allows us to study the properties of tetrameric and dimeric motors cross-linking polar-aligned and antialigned MTs separately, giving four motor categories: dimeric/polar-aligned, dimeric/antialigned, tetrameric/polar-aligned, and tetrameric/antialigned.

At each time step, motors attach at random positions, cross-linking beads of neighboring MTs at distances smaller than the threshold length d_t. A stretched motor of length d with spring stiffness k_m acts as a harmonic bond with energy, $V_m = k_m d^2/2$. The motor-arm of each motor moves on its respective MT with a constant velocity v_m until the stall length is reached ($d \geq d_s$). If the motor extension is larger than d_t, both motor-arms detach simultaneously. A detailed description of motor attachment, detachment, and motion rules is given in Supporting Material.

Parameters

We introduce dimensionless parameters using MT diameter r_{min}, thermal energy $k_B T$, and typical activity timescale τ, which indicates the onset of MT dynamics because of motors, as the basic length, energy, and timescales. Our simulations depend on eight dimensionless parameters: MT area fraction $\phi = N_f r_{\mathrm{eff}} L / \pi R_W{}^2$, MT aspect ratio L/r_{min}, confinement radius R_W/L, motor concentration N_m/N_f, maximum motor speed $v_m \tau / r_{\mathrm{min}}$, maximum motor extension d_t/r_{min}, motor stall force $f_s r_{\mathrm{min}}/k_B T$, and motor spring constant $k_m d_t / fs$.

We have studied structure and dynamics of MTs as a function of area fraction, confinement radius, motor spring constant, and motor velocity. In the main text, we have only varied the level of MT attraction, E_A and N_m/N_f, and kept the other parameters constant. We use $\phi = 0.74$ and $R_W/L = 8$ to demonstrate typical structures observed, while simultaneously keeping numerical costs low. The motor spring constant and motor speed used in the main text are motivated by biological values (Table S1). A complete list of simulation parameters and dimensionless groups used in our simulations is given in the Supporting Material. The description of our results for the dynamics of the MT-motor system for other parameter combinations is also deferred to the Supporting Material.

Dynamics

MTs are subject to force, $\boldsymbol{F}_i$; torque, $\boldsymbol{T}_i$ (Fig. 1); and anisotropic friction, $\boldsymbol{\Gamma}_i$. Hydrodynamic interaction of each MT with the background fluid is modeled using resistive-force theory; long-range hydrodynamic interactions between MTs are ignored (52). We use overdamped Brownian dynamics, i.e., the momenta of the MTs lose their memory and relax to thermal equilibrium between consecutive time intervals, δt (53). MTs obey the dynamical equations for translation and rotation,

$$\boldsymbol{r}_i(t+\delta t) = \boldsymbol{r}_i(t) + \boldsymbol{\Xi}_i^{-1}(t) \cdot \boldsymbol{F}_i(t)\delta t + \delta \boldsymbol{r}_i(t) \qquad (2)$$

and

$$\boldsymbol{p}_i(t+\delta t) = \boldsymbol{p}_i(t) + \gamma_r^{-1}[\boldsymbol{T}_i(t) \times \boldsymbol{p}_i]\delta t + \delta \boldsymbol{p}_i(t), \qquad (3)$$

respectively. The inverse friction tensor, $\Xi_i^{-1}(t)$, is orientation dependent and is given by

$$\Xi_i^{-1}(t) = \gamma_{\|}^{-1}\boldsymbol{p}_i(t)\boldsymbol{p}_i(t) + \gamma_{\perp}^{-1}[\boldsymbol{I} - \boldsymbol{p}_i(t)\boldsymbol{p}_i(t)], \quad (4)$$

where $\gamma_{||}$, $\gamma_{\perp}$, and γ_r are the parallel, perpendicular, and rotational friction coefficients of the MT, respectively. $\boldsymbol{F}_i$ and $\boldsymbol{T}_i$ are the sums of deterministic forces and torques on MT i, respectively, i.e., the forces and torques due to motors, steric forces from neighboring MTs, and steric repulsion from the confining wall. From hydrodynamics, the following expressions for long hard spherocylinders can be derived: $\gamma_{||} = \gamma_0 L$, $\gamma_{\perp} = 2\gamma_0 L$, and $\gamma_r = \gamma_0 L^3/6$. The friction coefficients are a function of the solution viscosity and the MT's aspect ratio (54). For the purpose of this simulation, γ_0 is constant for all three friction coefficients, because for the chosen aspect ratios the correction term for γ_0 is approximately equal for all three cases.

The Gaussian-distributed random displacements, $\delta\boldsymbol{r}_i(t)$, and rotations, $\delta\boldsymbol{p}_i(t)$, are related to the friction tensors by the fluctuation-dissipation theorem. The anisotropic random displacement and random reorientation vector have the variances

$$\langle \delta\boldsymbol{r}_i(t)\delta\boldsymbol{r}_i(t)\rangle = 2k_BT\Xi_i^{-1}\delta t, \quad (5)$$

and

$$\langle \delta\boldsymbol{p}_i(t)\delta\boldsymbol{p}_i(t)\rangle = 2k_BT\gamma_r^{-1}[\boldsymbol{I} - \boldsymbol{p}_i(t)\boldsymbol{p}_i(t)]\delta t. \quad (6)$$

The overall hybrid Brownian dynamics procedure is detailed in the Supporting Material.

RESULTS

Global structure

Fig. 3 shows the effect of MT attraction and motor type on the structures formed by confined MTs. The snapshots correspond to the lowest and highest E_A values (0.2 and 1.0 k_BT) probed in our simulations. In Fig. 3 *A*, stationary configurations reached by simulations without motors are shown. In the case without motors, structures form only because of steric interaction between MTs and geometric frustration induced by the boundary. For weak attractions ($E_A = 0.2\ k_BT$), we observe nematic ordering of MTs at the center of the confinement giving rise to defects at the edge of the confinement (Movie S1). Stronger attraction ($E_A = 1.0\ k_BT$) induces the formation of strong local alignment (but not polar order) that forms a more regular tiling pattern of MT stacks. We call these structures "bundles".

Dimeric motors (Fig. 3 *B*) lead to the formation of large polarity-sorted clusters, in which the average polarity changes smoothly (Movies S2 and S3), and bundles are not observed even for the largest MT attraction values. For the higher attraction energy, at stationary state, we observe relative sliding between both polar-aligned and antialigned MTs, meaning that the motor forces are stronger than attraction forces and bundles of MTs are broken up.

Tetrameric motors (Fig. 3 *C*) bring about a motor-induced polarity sorting mechanism as well (Movie S4). However, as explained in Fig. 2 and the Supporting Material, only motors that cross-link antialigned MT pairs induce large forces that slide MT pairs relative to each other. As a result, antialigned MTs are kinetically disadvantaged and are quickly removed from the system. In contrast to the case of dimeric motors, polar-aligned bundles are preserved because motors do not develop large sliding forces between polar-aligned MTs. Under high MT-MT attraction, multiple large bundles make up the entire system. Besides that, a larger-scale polar

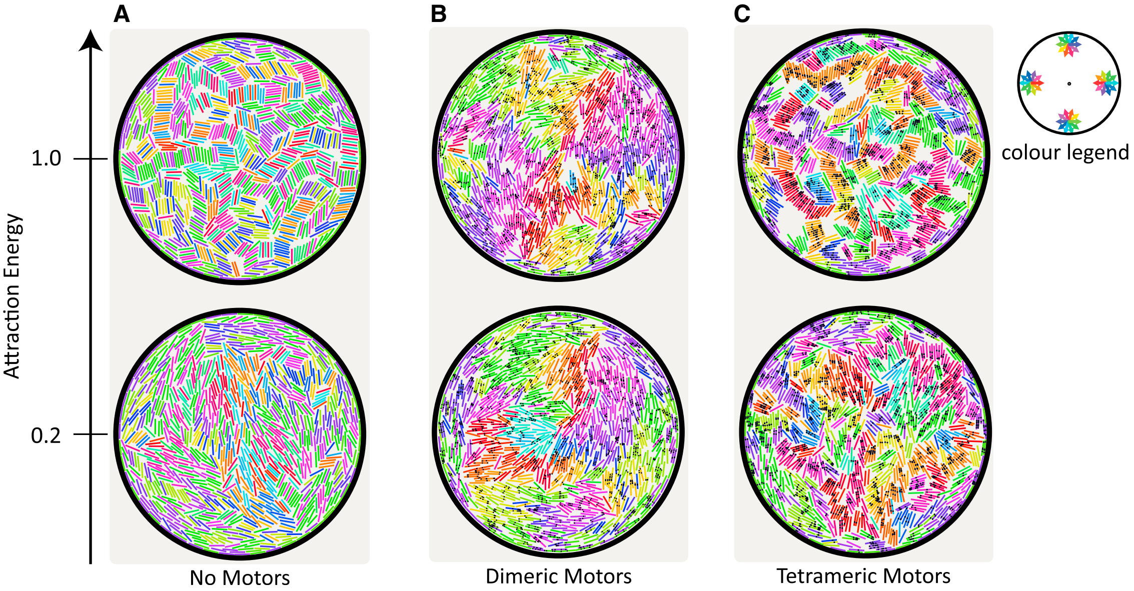

FIGURE 3 Stationary configuration of MTs with (*A*) no motors, (*B*) dimeric motors, and (*C*) tetrameric motors within circular confinement for two attraction energies, $E_A = 0.2\ k_BT$ and 1.0 k_BT. Number of motors is equal to the number of MTs for the four cases with motors, i.e., $N_m/N_f = 1$. Colors of MT represent their orientation with respect to the radial direction from the center. Small black dots represent the position of each motor-arm on MTs. For $E_A = 0.2\ k_BT$; (*A*), (*B*), and (*C*) correspond to Movies S1, S2, and S4, respectively. To see this figure in color, go online.

order is absent. The density of MT packing is increased due to the combined cohesive effect of the attractive potential and the presence of motors. For low MT-MT attraction, we observe that bundles are not as prevalent as in the case of higher attraction.

With increasing area fraction of MTs, due to higher pairwise MT sliding and steric interactions, polarity sorting becomes more prominent, and polar-aligned structured domains become more pronounced for both types of motors (Fig. S6). The number of these domains increases with R_W/L (Fig. S8). The steady-state global structures are generally preserved for values of $k_m d_t / f_s$ (Fig. S12) and $v_m \tau / r_{\min}$ (Fig. S14) close to biologically motivated values.

The timescale for the formation of self-organized structures due to dimeric and tetrameric motors, beginning from an equilibrated, passive configuration, can be estimated from the relaxation of the polar order parameter. The time taken for polarity sorting shortens with increasing motor concentration (Fig. S19). Also, sorting occurs faster in tetrameric motor systems than in dimeric motor systems for all motor concentrations, due to higher motor stresses generated by tetrameric motors for antialigned MT pair configurations.

Local polar order

The dynamics of individual MTs depends on the polar orientation of MTs in their local environment. To capture the notion of the polarity of the local environment around a given MT i, we define a local polar order parameter,

$$\psi_i = \frac{\sum_{j \neq i}^{N} \boldsymbol{p}_i \cdot \boldsymbol{p}_j q_{ij}}{\sum_{j \neq i}^{N} q_{ij}}. \tag{7}$$

Here, q_{ij} is the pairwise motor partition function that weights a MT pair consisting of MT i and MT j according to the stretching energy of a uniform distribution of motors cross-linking the two MTs (21). The local polar order parameter ψ_i ranges from -1 (MT i is surrounded by neighbors in the opposite orientation) to 1 (MT i is surrounded by neighbors of same orientation). The precise definition of q_{ij} and a discussion of the local polar order parameter is given in the Supporting Material.

Fig. 4 shows the probability of finding an MT with the local order parameter, ψ. Steric interactions cause MTs to orient parallel to each other, such that most MTs have ψ_i values close to -1 or 1. Passive systems cannot distinguish between polar-aligned and antialigned orientations, implying that either orientations are equally probable. Both types of molecular motors induce an effective polarity sorting, breaking the symmetry between these two orientations. As a consequence, most MTs are in the polar-aligned orientation, and not in the antialigned orientation. For all values of the attraction energy E_A, there is a slightly higher fraction of antialigned MTs in the dimeric motor system than the tetrameric motor system (Fig. 4, *inset*).

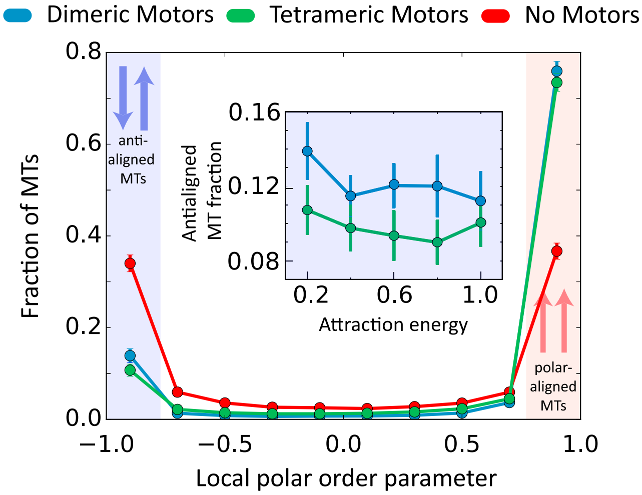

FIGURE 4 Fraction of MTs in the system as a function of their local polar order parameter for the $E_A = 0.2\ k_B T$, $N_m/N_f = 1$ systems. Inset (*blue*) shows the fraction of antialigned MTs in systems as a function of different E_A values for $N_m/N_f = 1$. Attraction energy is normalized by $k_B T$. To see this figure in color, go online.

Motor-mediated motion

The local polar order parameter gives a structural description of the MT environment. To quantify the influence of local polar order on MT dynamics, we investigate it at two regimes separated by a crossover time τ (Fig. 5). At short timescales, the MT motion is driven by the thermal bath. At large timescales, collective interaction between multiple MTs takes place. At timescales comparable to τ, stresses generated by the motors are dissipated in the thermal bath. We define the mean squared displacement (MSD) of the MTs' centers of masses using

$$\mathrm{MSD}(t') \equiv \left\langle \left| \boldsymbol{r}_i(t) - \boldsymbol{r}_i(t+t') \right|^2 \right\rangle_{t,\, i}, \tag{8}$$

where t' is the lag time. The characteristic lag time, $t' = \tau$, is chosen such that the MTs' MSD is just out of the diffusive regime for the dimeric motor system, with $N_m/N_f = 2.0$ and $E_A = 0.2\ k_B T$. At lag times smaller than τ, Fig. 5 shows that MTs are diffusing, because MSD/(lag time) is constant. At lag times larger than τ, systems with motors cause MTs to displace actively, and activity increases with the concentration of motors. In this time regime, steric interactions with neighboring MTs become dominant, because MSD of MTs without motors shows a decrease in diffusion. The peaks in Fig. 5 *A*, at large timescales, indicate that MTs are hindered by the confinements and the squared displacements are limited by confinement size. The MSD plateaus approximately at ${R_W}^2$ for lag times larger than

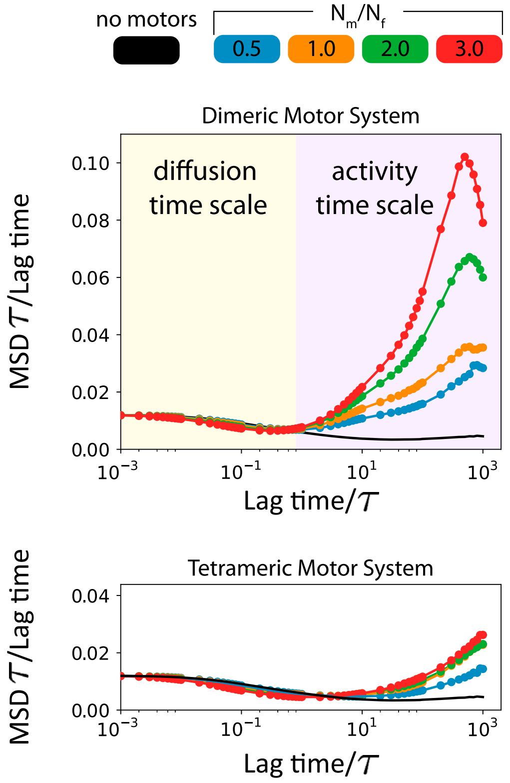

FIGURE 5 Translational MSD/lag time of MTs' center of masses for dimeric motors (A) and tetrameric motors (B) for different motor concentrations, N_m/N_f. The y axis scale for (A) and (B) are the same to show the differences in dynamics between the two systems. MSD is normalized using L^2 and lag time is normalized using the onset of the activity timescale, τ, i.e., the lag time where motor stresses are manifested in the MT dynamics. $E_A = 0.2\ k_BT$ for all simulations. To see this figure in color, go online.

$10^3\ \tau$, because a significant proportion of MTs have displaced the confinement radius, and are obstructed. This effect results in the curves in Fig. 5 decreasing (to 0) despite the motor-induced activity. A comparison of Fig. 5, A and B, which are both plotted on the same scale, shows that in these timescales, MTs driven by dimeric motors are significantly more dynamic than MTs driven by tetrameric motors for all motor concentrations. However, note that the velocities of MTs depend strongly on $k_m d_t/f_s$ (Fig. S13) and $v_m\tau/r_{\mathrm{min}}$ (Fig. S15), and less on MT area fraction and confinement size.

Having defined a characteristic lag time, τ, we now define an effective MT velocity,

$$\boldsymbol{v}(t) = \frac{\boldsymbol{r}(t+\tau/2) - \boldsymbol{r}(t-\tau/2)}{\tau}. \tag{9}$$

We compute an effective, average MT propulsion velocity due to motor stresses, $v_{||}$, by projecting $\boldsymbol{v}(t)$ on $\boldsymbol{p}(t)$.

Fig. 5 shows that on average the dimeric motors induce significantly larger displacements than tetrameric motors, despite having only half of the mobility of the tetrameric motors. This is contrary to the case of a single pair of MTs that was intuited in Fig. 2. Doubling the number of motors also induced larger displacements in the dimeric motor system.

Furthermore, for both dimeric and tetrameric motors, Fig. 6 shows that the MT velocity is strongly correlated with the polarity of its environment, with highest propulsion velocities measured for MTs antialigned with respect to their environments. Velocities generated by the two types of motors depend also on the MTs' attraction energy E_A (Fig. 6 *inset*). Namely, tetrameric motors are less able to overcome attractive forces that favor bundle formation (Fig. S3 B), relative to dimeric motors. At $E_A = 0.2\ k_BT$, dimeric motors induce antialigned parallel MT velocity only 1.2 times that induced by tetrameric motors. At $E_A =$ 0.2 k_BT, however, a relative decrease in MT velocities is found in the tetrameric motor system. At this higher level of attraction, mean parallel MT velocity induced by dimeric motors is 1.9 times the velocity induced by the tetrameric motors.

Fig. 7 shows histograms of parallel velocities of MTs for polar-aligned and antialigned MTs (local polar order parameter close to +1 and −1, respectively). The histogram without motors shows the effect of thermal forces at this timescale. Dimeric motors that cross-link polar-aligned MT pairs also cause a parallel MT velocity distribution that is centered around zero, but has a larger width than the passive MTs. Antialigned MTs and polar-aligned MTs cross-linked by dimeric motors have a velocity distribution

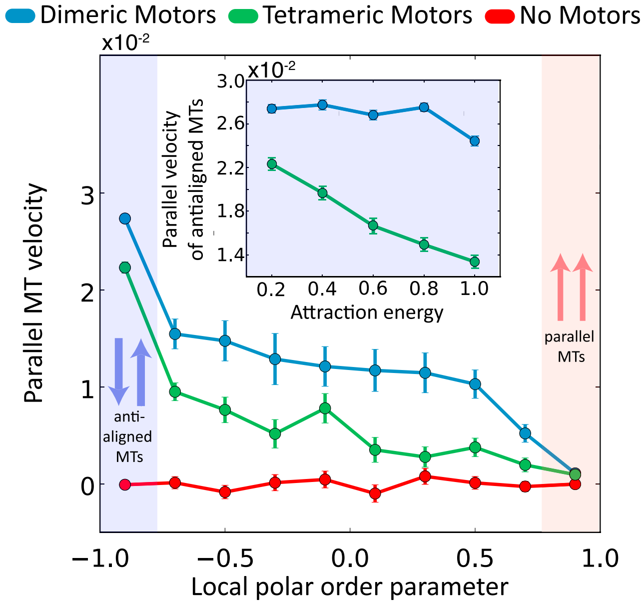

FIGURE 6 Parallel velocities as a function of local polar order parameter for $E_A = 0.2\ k_BT$ systems and $N_m/N_f = 1$. Inset (*blue*) shows the velocity of antialigned MTs in systems with different E_A values for $N_m/N_f = 1$. Because motor-arms move in the opposite direction of $\boldsymbol{p}$, by this convention, a propelled MT moves in the opposite direction, giving positive values for $v_{||}$. Velocities are normalized by L/τ. Attraction energy is normalized by k_BT. To see this figure in color, go online.

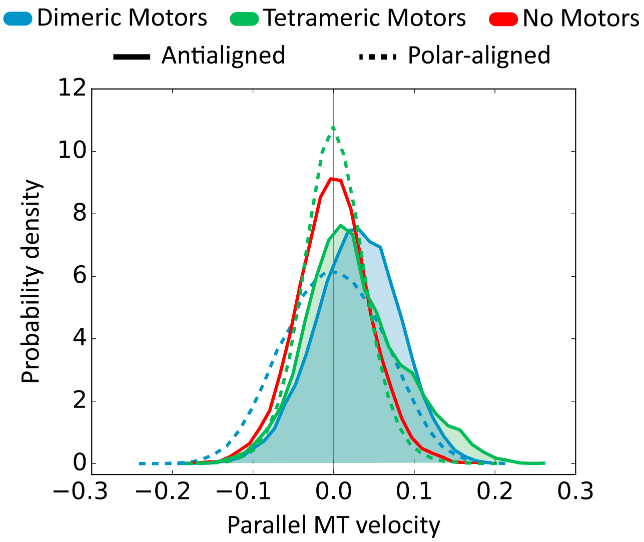

FIGURE 7 Histogram of parallel velocities for antialigned and polar-aligned MTs from the antialigned bins (*blue*) and the polar-aligned bins (*red*) from Fig. 6 ($E_A = 0.2\ k_BT$ and $N_m/N_f = 1$). Table 1 shows the first three moments of the distribution. The areas under the curve from antialigned MTs in dimeric and tetrameric motor systems are colored blue and green, respectively. The black vertical line represents a parallel MT velocity of zero. Velocities are normalized by L/τ. To see this figure in color, go online.

that corresponds to scenarios posited in Fig. 2, *D* and *F*, and Fig. 2, *C* and *E*, respectively. Both antialigned MT mechanisms in Fig. 2, *D* and *F*, give an effective propulsion in the direction of MT orientation, which results in the skewed velocity distribution, and the peak of the velocity is nonzero (Table 1). Both polar-aligned MT mechanisms in Fig. 2, *C* and *E*, are impervious to the MT orientations, and result in motor-induced motion in either direction, depending on the location of the anchored arm(s). This results in a symmetric distribution of velocities shown in Fig. 7, which has a wider distribution of velocities than both polar-aligned tetrameric motor and passive MT systems.

Tetrameric motors that cross-link polar-aligned MT pairs lead to bundle formation that results in a narrower velocity distribution. In general, MTs in antialigned environments have a skewed velocity distribution compared to the polar-aligned MTs due to sliding motor stresses. The manner by which this sliding force manifests is different for dimeric and tetrameric motors.

As posited, the relative longitudinal displacement and the resultant maximal force for tetrameric motors is higher than for dimeric motors. However, on average, antialigned MT pairs are propelled more by dimeric motors than by tetrameric motors. Although tetrameric motors between antialigned MTs are able to generate higher velocities, these only make up the tail of the positively skewed distribution (Table 1). Dimeric motors, on the other hand, have the peak of their distribution at a higher velocity than that of tetrameric motors, and the distribution is skewed in the opposite direction.

TABLE 1 First Three Moments for the Parallel MT Velocity Distribution from Fig. 7

Motor Type	MT Orientation	Mean	SD	Skew
Dimeric	antialigned	0.029	0.052	−0.154
	polar-aligned	−0.001	0.061	−0.003
Tetrameric	antialigned	0.025	0.060	0.405
	polar-aligned	−0.001	0.040	0.092
No motors	—	0.000	0.045	0.012

Dynamics near confinement

So far, we have compared differences in overall structure and dynamics of confined MT ensembles for dimeric and tetrameric motors. Having established that the dimeric motor system is the more dynamic of the two systems, to understand collective effects of motile MTs, we study how motion is coordinated within the confinement by dimeric motors. Fig. 8 shows trajectories of four especially motile probe MTs (*orange*, *green*, *yellow*, and *blue*) and the environment upon which they conduct this motion.

The MTs travel with higher velocities in an environment of antialigned MTs and show erratic motion in an environment of polar-aligned MTs. If they encounter defects at the boundary (55), such as the blue MT at 500τ in Fig. 8, their trajectory may change direction abruptly.

Persistent motion is most prevalent at the edge of the confinement for both dimeric and tetrameric motors (Fig. 9). The parallel MT velocities are higher near the circular boundaries, whereas MTs have small velocities in the center of the confinement for radii below 0.7 R_W. Velocities at the boundary are significantly higher for dimeric motor systems than for tetrameric motor systems (Fig. S22). Parallel MT velocity near the boundary generally decreases with increasing MT attraction. This is due to the lack of MT activity with cohesive interactions that hinder MT-MT sliding (Fig. 9, *inset*).

Motor evolution

We define motor processivity as the number of consecutive time steps that a motor remains attached without releasing the cross-linked MT pair, i.e., the youngest (oldest) motors with the lowest (highest) processivity are the motors that have been attached for the shortest (longest) period of time. In our simulations, a motor that does not reach stall length will have motor-arms that each cover MT length *L* in 10τ.

Fig. 10 *A* shows that the youngest motors are the most numerous, and the number of motors decreases exponentially with processivity, i.e., motors detach from MT pairs at a rate proportional to the number of surviving motors. Tetrameric motors that cross-link antialigned MTs have the fastest detachment rate and the shortest mean lifetime (Fig. 10 *B*; Table 2). The rate of detachment and the mean

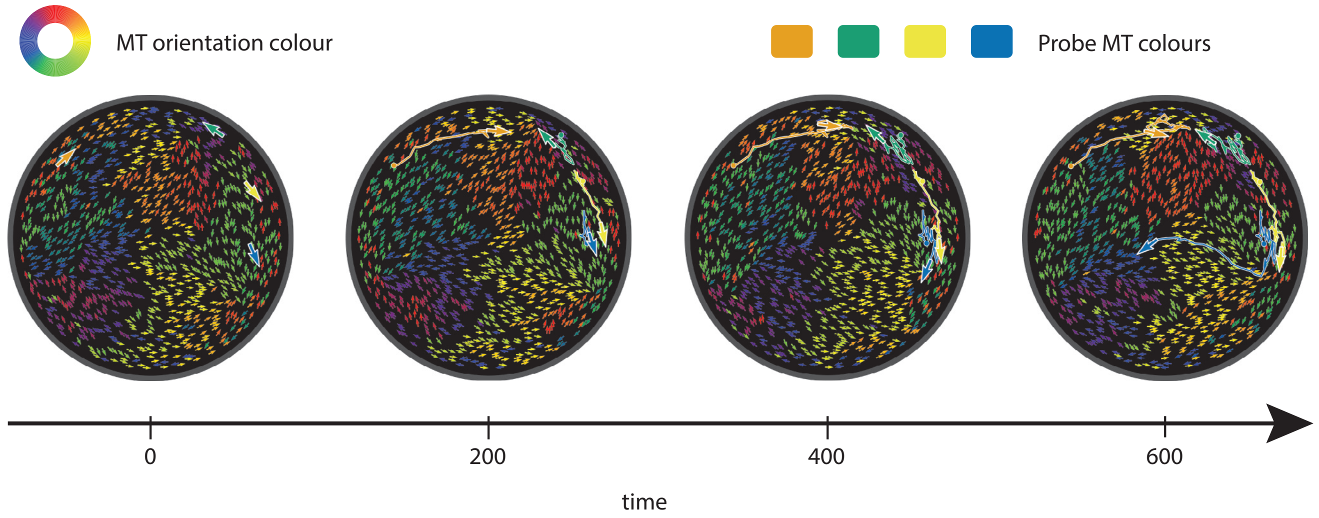

FIGURE 8 Time-lapse images of MTs in a dimeric motor system, with probe MTs represented with larger arrows and their trajectories plotted in orange, green, yellow, and blue. Smaller arrows represent all the other MTs. All arrows indicate the direction of vector $\boldsymbol{p}$, i.e., the opposite direction of motor motion, which is generally the direction of MT propulsion. The trail left by the larger arrows corresponds to the path that they have taken. In this case, $E_A = 0.2$ and $N_m/N_f = 1$. The time axis is normalized using τ. The images correspond to Movie S5. To see this figure in color, go online.

lifetime in the other three cases are similar. Because the probability of motor attachment is independent of MT alignment and there are fewer antialigned MT pairs than polar-aligned MT pairs, motors between antialigned MTs are fewer than motors between polar-aligned MTs (Fig. 10 *A*, *inset*). From Fig. 10 *B*, we see that the average motor extensions are distributed similarly about a mean of $0.65d_t$. It also shows that the contribution of energy from the motors comes mostly from motors cross-linking polar-aligned MTs, especially for the system with tetrameric motors (Table 2), because motors cross-linking antialigned MT pairs are less processive, and fewer in number. We also observe that motor extension decreases linearly with processivity. The relationship between motor extension and motor processivity is similar between all motors, except the tetrameric motors that cross-link antialigned MTs. At $N_m/N_f = 1$, one-half of the dimeric motors were lone motors connecting MT pairs and of the remaining motors, 70% of the motors were in a correlated orientation, i.e., with their motile (anchored) arms on the same MT.

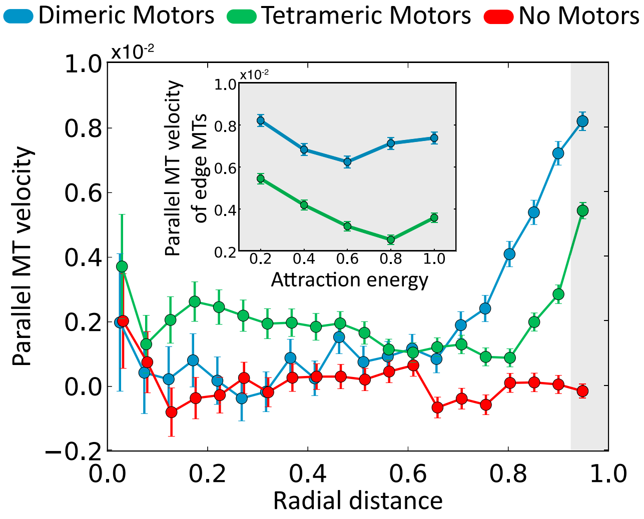

FIGURE 9 Parallel velocities of MT systems with tetrameric, dimeric, and no-motors as a function of radial distance for $E_A = 0.2\ k_BT$ and $N_m/N_f = 1$. Inset (*shaded*) shows the mean velocity of the MTs closest to the confinement edge for different E_A values for $N_m/N_f = 1$. Velocities are normalized by L/τ. Radial distance is normalized by confining wall radius, R_W. Attraction energy is normalized by k_BT. To see this figure in color, go online.

With increasing motor velocity, particularly in the dimeric motor system, the system becomes more dynamic due to larger sustained active stresses. At high motor velocities ($v_m\tau/r_{\min} > 50$), tetrameric motors connecting antialigned MTs have significantly lower motor processivity than dimeric motors, which is required to sustain large active stresses (Fig. S20). This is because, at higher motor velocities, motors exceed their threshold length before MTs can respond to the stretched motor.

At low motor velocities ($v_m\tau/r_{\min} = 5$), MT polarity sorting takes much longer. At a timescale of τ, slow motors behave as passive cross-linkers and hinder diffusion (Fig. S15).

DISCUSSION

Cellular-level processes, such as cytoplasmic streaming, require molecular level characterization and the unification of complex biomolecular systems across length and timescales. Motile systems can be studied either by ignoring microscopic mechanisms and focusing on macroscopic properties, or just measuring the microscopic properties

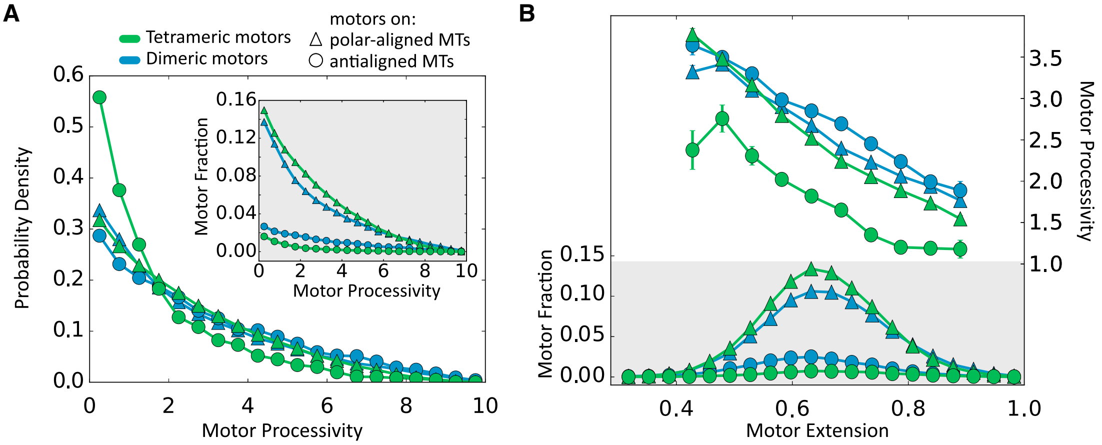

FIGURE 10 (*A*) Histogram of motor processivity for the four motor categories (dimeric/polar-aligned, dimeric/antialigned, tetrameric/polar-aligned, and tetrameric/antialigned). Inset (*shaded*) is the histogram before normalization. (*B*) Histograms (not normalized) of motor extensions, and motor processivity as a function of motor extension. Parameters are $E_A = 0.2$ and $N_m/N_f = 1$. Motor processivity is normalized using the timescale, τ. Motor extensions are normalized using motor threshold extension, d_t. To see this figure in color, go online.

of individual components. We have taken a step toward capturing cellular-scale phenomena by marrying three distinct length scales: 1) molecular motors, the smallest elements; 2) MTs, the major components whose activity is of main interest; and 3) the confining wall, the largest length scale. By subjecting confined MTs to dimeric and tetrameric motors under different levels of MT-MT attraction, we observe a variety of large-scale structures in two dimensions. Although real cells are intrinsically 3D, our simulations should be relevant to experiments that study cytoplasmic streaming within a plane for cells that are attached to a substrate. Moreover, our simulations directly apply to experimental 2D model systems of cytoskeletal filaments (13–15), and extend previous theoretical and simulation studies of MT-motor systems (19,21,23).

The structures observed in the case of passive MTs under low attraction are consistent with calculations based on the generalized Onsager model, where ordered twofold symmetric defect structures are observed between nonattractive filaments within a line boundary at high densities (56). In this model, activity mediated by dimeric motors led to large polar-aligned MT clusters that were nonmotile at short timescales. Tuning MT-MT attraction levels to those prescribed in experiments did not have a significant effect on the structure of this system (47). MTs subject to tetrameric motors formed small polar-aligned bundles, and increasing MT-MT attraction enhanced MT bundling in these systems. Bundling of MTs subject to tetrameric motors were similarly observed in cases of high motor concentration and small motor run lengths in 2D simulations of a minimal physical model of MTs, motors, and static cross-linkers (19). Similar bundles were also reported in simulations of active gels of filaments and motors between two infinite parallel walls, at high motor attachment rates (23).

In computer simulations of a filament-motor system confined to a pressurized cylindrical box, where the confinement radius was slightly larger than the length of a semiflexible filament, rotational motion of filaments and motors during a transient vortex phase was observed (24). This system ultimately collapsed into a semiaster. In contrast, for our circular confinement with a radius eight times the MT length, we find persistent flows close to the confinement wall. Although the large polar-aligned clusters in the case of the dimeric motors do not exhibit significant short-time dynamics (Fig. 9), fluctuations in MT orientations within these clusters close to the confining wall gives antialigned MTs that result in persistent flows and redistribution of MTs throughout the confinement. This activity can be seen in the velocities of MTs in antialigned environments and their trajectories.

With filament lengths comparable to the radius of the confinement, two +1/2 defects were observed at the confinement edge in both active (24) and passive (56) cases. We recovered such defects in passive cases. However, with shorter filaments relative to confinement radius, defects were not distinguishable in the tetrameric motor systems, and multiple +1/2 defects were observed in the dimeric motor system close to the confinement, and conjugate −1/2 defects in the bulk (Fig. S8). We posit that a sufficiently flexible boundary can lead to filopodia-like protrusion, which will be actively extended by the +1/2 defect tip, as

TABLE 2 Mean Motor Lifetimes are Obtained from Fitting Exponential Curves to Fig. 10 *A*

Motor Type	MT Orientation	Mean Lifetime	Motor Energy Fraction
Dimeric	polar-aligned	2.87	0.789
	antialigned	3.58	0.211
Tetrameric	polar-aligned	3.05	0.936
	antialigned	1.51	0.064

Motor energy fraction is the sum of squared lengths of motors cross-linking polar-aligned (antialigned) MTs relative to all the motors in the system. Mean lifetime is normalized using the timescale, τ.

observed in experiments where MTs are confined to the surface of a spherical vesicle (15).

We have shown that motor-mediated pairwise interactions give large-scale MT dynamics. The polarity sorting mechanism, where motors induce cohesive interactions between polar-aligned MTs, and larger forces between antialigned MTs, have been previously observed and described in various studies (19,21,25). Similarly, we show that MTs move persistently in a direction coupled with their polarity, i.e., in the opposite direction of motor-arm motion. Motors that cross-link aligned and antialigned MTs give symmetric and asymmetric longitudinal displacements of MTs in Fig. 7. Although, in another simulation of MT-motor mixtures, a linear force-velocity dependence for motor velocity is used (21), our simulations give symmetric and asymmetric longitudinal displacement profiles for motors cross-linking aligned and antialigned MTs, respectively.

To disentangle the effect of motors with two active arms, and one active arm and an anchored arm, we keep the active motor arm's stepping rate constant, unlike in other MT-motor studies (19,21,25). In comparison with (21), which observes longer extensions for motors cross-linking antialigned MTs, we observe a similar and symmetric motor extension profile across all types of motors Fig. 10 *B*. This is because in our model, motors cross-link MTs at a constant rate regardless of their extension (below the motor threshold length). In (21), extension of motors upon attachment is determined by a semigrand canonical ensemble approach. Nevertheless, in our work, motor processivity of motors cross-linking antialigned MTs is smaller for tetrameric motors, as was also found in (21). In general, between the two agents of dipolar force (tetrameric and dimeric motors), we observe that the dimeric motors are more effective at inducing large forces between antialigned MTs.

In our simulations, the attractive wall leads to a layer of less motile, disordered MTs near the wall. This may model a cortical actin cytoskeleton to which motors can cross-link and propel MTs in the bulk. In vivo experiments have shown that a network of stable MTs are anchored to the actin cortex near the cell membrane and that a directed streaming process is carried out by the motors that use these anchored MTs as tracks to propel cytoplasmic MTs (5). These experiments indicate that cytoplasmic MTs travel five times faster than the anchored, cortical MTs; also, cells with kinesin mutants deficient in MT sliding resulted in a 14-fold decrease in cytoplasmic MT velocities under the particular conditions of these experiments. In our simulations, relative to the MTs at the center of the confinement, wall attraction causes a threefold and 1.4-fold increase in parallel MT velocity at the confinement edge for the tetrameric and dimeric motor systems, respectively (Fig. S18). We conclude that the overall dynamics of the system is enhanced by motor asymmetry, and that this is most prominent close to the edge of the confinement (Fig. S22), due to the layer of immobile MTs at the confinement wall.

By comparing dimeric motors with tetrameric motors, we have studied the role of asymmetry of motor-arm velocity in propagating MT motility within confinement. The tetrameric motor model has been considered extensively in computer simulations to describe similar phenomena (19,21,23), but the effect of motor asymmetry has been largely ignored, despite its ubiquity in nature to propagate MT-MT sliding. Apart from the role of the dimeric motor, kinesin-1, in streaming systems in nature (5,9,10), computer simulations that investigated force generation in 1D bundles of MTs (34) report bundle expansion only in the case of dimeric motors. Tetrameric motors, on the other hand, opposed bundle expansion. In fact, it has been shown that the regulation of axon initiation and growth can only be explained by considering the significant roles of dimeric motors such as kinesin-1 and cytoplasmic dynein (34), on top of MT polymerization. The extensile nature of the aligned 1D filament bundles is reflected by the elongated clusters in our simulations.

Differences in MT motion as a result of motor asymmetry are not immediately obvious. For instance, higher sliding velocities between antialigned MTs cross-linked by tetrameric MTs, due to a higher longitudinal displacement per time step, as depicted in Fig. 2, may be expected. However, we have shown that, on average, antialigned MTs cross-linked by dimeric motors slide faster, and that the higher velocities of the tetrameric motors only make the tail of a skewed parallel MT velocity distribution (Fig. 7; Table 1). The dimeric motors, although incapable of producing as large forces as tetrameric motors, could sustain a larger force for a longer time without detaching, resulting in a more symmetric parallel MT velocity distribution with a larger absolute mean velocity (Fig. 10).

We find that the dynamics of MTs is strongly dependent on the local polar order parameter, i.e., the density of opposite-polarity MTs. This supports simulation results for 1D filament bundles cross-linked by molecular motors, where the drift rate for a given filament has been shown to be a linear function of the density of the opposite-polarity filaments (35). This further consolidates general assumptions made by polarity-dependent continuum models of MTs (57), where interaction between antiparallel filaments phenomenologically leads to filament sorting. Our simulations identify the mechanisms involved (Fig. 2) that contribute to the distribution of parallel MT velocities for dimeric and tetrameric motors.

In reconstituted systems of MTs in vitro (14), biotin-labeled kinesin motors have been conjugated using streptavidin clusters, and applied to a mixture of MTs condensed onto an oil-water interface. Based on MT structures observed in these experiments, we hypothesize that such a system of motors can be modeled using dimeric motors. In vitro motility assays have shown that conventional kinesin motors are processive, i.e., single molecules of kinesin move continuously along a MT for several microns (58,59). Biochemical experiments have confirmed that kinesin molecules hydrolyze on average 125 molecules of ATP after binding to a MT, consistent with the motor taking 125 8-nm steps (60). When such a processive motor is paired to a motor that is in the rate-limiting nonmotile state (61), the stress generated between MTs will be different from that between MTs connected by a tetrameric motor, which has two fully active arms. From our system, it is clear that the asymmetry in motor-arm motion greatly aids MT activity and the extensile sliding between MTs. Hence, such a model with asymmetric motor-arm motion might be more suited to give a microscopic explanation to the extensile behavior of MT bundles.

In the future, we intend to include semiflexibility of MTs to capture dynamics of MT bundles instead of individual MTs. By simulating larger length scales, we expect to substantiate defect dynamics with accurate microscopic mechanisms for MT bundle extension.

SUPPORTING MATERIAL

Supporting Materials and Methods, twenty-two figures, two tables, and five movies are available at http://www.biophysj.org/biophysj/supplemental/S0006-3495(17)30841-X.

AUTHOR CONTRIBUTIONS

A.R., G.A.V., G.S., T.A., and G.G. designed the study. A.R. performed the simulations and analyzed the data. All authors discussed and interpreted results. All authors wrote the manuscript.

ACKNOWLEDGMENTS

We thank T. Eisenstecken, S. Das, and Ö. Duman for helpful discussions.

A.R. gratefully acknowledges financial support from the Otto-Bayer Fellowship Program. The authors gratefully acknowledge the computing time granted by the John von Neumann Institute for Computing (NIC) and provided on the supercomputer JURECA at Jülich Supercomputing Centre (JSC).

SUPPORTING CITATIONS

References (62–66) appear in the Supporting Material.

REFERENCES

1. Urrutia, R., M. A. McNiven, …, B. Kachar. 1991. Purified kinesin promotes vesicle motility and induces active sliding between microtubules in vitro. *Proc. Natl. Acad. Sci. USA.* 88:6701–6705.
2. Straube, A., G. Hause, …, G. Steinberg. 2006. Conventional kinesin mediates microtubule-microtubule interactions in vivo. *Mol. Biol. Cell.* 17:907–916.
3. Tanenbaum, M. E., R. D. Vale, and R. J. McKenney. 2013. Cytoplasmic dynein crosslinks and slides anti-parallel microtubules using its two motor domains. *eLife.* 2:e00943.
4. Astumian, R. D. 2012. Microscopic reversibility as the organizing principle of molecular machines. *Nat. Nanotechnol.* 7:684–688.
5. Lu, W., M. Winding, …, V. I. Gelfand. 2016. Microtubule-microtubule sliding by kinesin-1 is essential for normal cytoplasmic streaming in *Drosophila* oocytes. *Proc. Natl. Acad. Sci. USA.* 113:E4995–E5004.
6. Theurkauf, W. E. 1994. Microtubules and cytoplasm organization during *Drosophila* oogenesis. *Dev. Biol.* 165:352–360.
7. Serbus, L. R., B.-J. Cha, …, W. M. Saxton. 2005. Dynein and the actin cytoskeleton control kinesin-driven cytoplasmic streaming in *Drosophila* oocytes. *Development.* 132:3743–3752.
8. Gutzeit, H. 1986. The role of microtubules in the differentiation of ovarian follicles during vitellogenesis in *Drosophila*. *Rouxs Arch. Dev. Biol.* 195:173–181.
9. Ganguly, S., L. S. Williams, …, R. E. Goldstein. 2012. Cytoplasmic streaming in *Drosophila* oocytes varies with kinesin activity and correlates with the microtubule cytoskeleton architecture. *Proc. Natl. Acad. Sci. USA.* 109:15109–15114.
10. Jolly, A. L., H. Kim, …, V. I. Gelfand. 2010. Kinesin-1 heavy chain mediates microtubule sliding to drive changes in cell shape. *Proc. Natl. Acad. Sci. USA.* 107:12151–12156.
11. Winding, M., M. T. Kelliher, …, V. I. Gelfand. 2016. Role of kinesin-1-based microtubule sliding in Drosophila nervous system development. *Proc. Natl. Acad. Sci. USA.* 113:E4985–E4994.
12. Nédélec, F. J., T. Surrey, …, S. Leibler. 1997. Self-organization of microtubules and motors. *Nature.* 389:305–308.
13. Sanchez, T., D. T. Chen, …, Z. Dogic. 2012. Spontaneous motion in hierarchically assembled active matter. *Nature.* 491:431–434.
14. DeCamp, S. J., G. S. Redner, …, Z. Dogic. 2015. Orientational order of motile defects in active nematics. *Nat. Mater.* 14:1110–1115.
15. Keber, F. C., E. Loiseau, …, A. R. Bausch. 2014. Topology and dynamics of active nematic vesicles. *Science.* 345:1135–1139.
16. Elgeti, J., R. G. Winkler, and G. Gompper. 2015. Physics of microswimmers—single particle motion and collective behavior: a review. *Rep. Prog. Phys.* 78:056601.
17. Jülicher, F., A. Ajdari, and J. Prost. 1997. Modeling molecular motors. *Rev. Mod. Phys.* 69:1269–1282.
18. Prost, J., F. Jülicher, and J.-F. Joanny. 2015. Active gel physics. *Nat. Phys.* 11:111–117.
19. Blackwell, R., O. Sweezy-Schindler, …, M. D. Betterton. 2016. Microscopic origins of anisotropic active stress in motor-driven nematic liquid crystals. *Soft Matter.* 12:2676–2687.
20. Kruse, K., J. F. Joanny, …, K. Sekimoto. 2004. Asters, vortices, and rotating spirals in active gels of polar filaments. *Phys. Rev. Lett.* 92:078101.
21. Gao, T., R. Blackwell, …, M. J. Shelley. 2015. Multiscale polar theory of microtubule and motor-protein assemblies. *Phys. Rev. Lett.* 114:048101.
22. Hiraiwa, T., and G. Salbreux. 2016. Role of turnover in active stress generation in a filament network. *Phys. Rev. Lett.* 116:188101.
23. Head, D. A., W. J. Briels, and G. Gompper. 2014. Nonequilibrium structure and dynamics in a microscopic model of thin-film active gels. *Phys. Rev. E Stat. Nonlin. Soft Matter Phys.* 89:032705.
24. Head, D. A., W. Briels, and G. Gompper. 2011. Spindles and active vortices in a model of confined filament-motor mixtures. *BMC Biophys.* 4:18.
25. Head, D. A., G. Gompper, and W. J. Briels. 2011. Microscopic basis for pattern formation and anomalous transport in two-dimensional active gels. *Soft Matter.* 7:3116–3126.
26. Ronceray, P., C. P. Broedersz, and M. Lenz. 2016. Fiber networks amplify active stress. *Proc. Natl. Acad. Sci. USA.* 113:2827–2832.
27. Marchetti, M. C., J. F. Joanny, …, R. A. Simha. 2013. Hydrodynamics of soft active matter. *Rev. Mod. Phys.* 85:1143–1189.
28. Palacios, I. M., and D. St Johnston. 2002. Kinesin light chain-independent function of the Kinesin heavy chain in cytoplasmic streaming and

posterior localisation in the *Drosophila* oocyte. *Development.* 129:5473–5485.

29. Braun, M., D. R. Drummond, …, A. D. McAinsh. 2009. The kinesin-14 Klp2 organizes microtubules into parallel bundles by an ATP-dependent sorting mechanism. *Nat. Cell Biol.* 11:724–730.
30. Schliwa, M. 2003. Molecular Motors. Wiley, Weinheim, Germany.
31. Hentrich, C., and T. Surrey. 2010. Microtubule organization by the antagonistic mitotic motors kinesin-5 and kinesin-14. *J. Cell Biol.* 189:465–480.
32. van den Wildenberg, S. M., L. Tao, …, E. J. Peterman. 2008. The homotetrameric kinesin-5 KLP61F preferentially crosslinks microtubules into antiparallel orientations. *Curr. Biol.* 18:1860–1864.
33. Arpağ, G., S. Shastry, …, E. Tüzel. 2014. Transport by populations of fast and slow kinesins uncovers novel family-dependent motor characteristics important for in vivo function. *Biophys. J.* 107:1896–1904.
34. Jakobs, M., K. Franze, and A. Zemel. 2015. Force generation by molecular-motor-powered microtubule bundles; implications for neuronal polarization and growth. *Front. Cell. Neurosci.* 9:441.
35. Zemel, A., and A. Mogilner. 2009. Motor-induced sliding of microtubule and actin bundles. *Phys. Chem. Chem. Phys.* 11:4821–4833.
36. Elgeti, J., and G. Gompper. 2013. Wall accumulation of self-propelled spheres. *Eur. Phys. Lett.* 101:48003.
37. Fily, Y., A. Baskaran, and M. F. Hagan. 2014. Dynamics of self-propelled particles under strong confinement. *Soft Matter.* 10:5609–5617.
38. Fily, Y., A. Baskaran, and M. F. Hagan. 2015. Dynamics and density distribution of strongly confined noninteracting nonaligning self-propelled particles in a nonconvex boundary. *Phys. Rev. E Stat. Nonlin. Soft Matter Phys.* 91:012125.
39. de Silva, M. S., J. Alvarado, …, G. H. Koenderink. 2011. Self-organized patterns of actin filaments in cell-sized confinement. *Soft Matter.* 7:10631–10641.
40. Gonzalez-Pinto, M., F. Borondo, …, E. Velasco. 2017. Clustering in vibrated monolayers of granular rods. *Soft Matter.* 13:2571–2582.
41. Théry, M., V. Racine, …, M. Bornens. 2005. The extracellular matrix guides the orientation of the cell division axis. *Nat. Cell Biol.* 7:947–953.
42. Fink, J., N. Carpi, …, M. Piel. 2011. External forces control mitotic spindle positioning. *Nat. Cell Biol.* 13:771–778.
43. Versaevel, M., T. Grevesse, and S. Gabriele. 2012. Spatial coordination between cell and nuclear shape within micropatterned endothelial cells. *Nat. Commun.* 3:671.
44. Verkhovsky, A. B., O. Y. Chaga, …, G. G. Borisy. 2003. Orientational order of the lamellipodial actin network as demonstrated in living motile cells. *Mol. Biol. Cell.* 14:4667–4675.
45. Goldstein, R. E., and J.-W. van de Meent. 2015. A physical perspective on cytoplasmic streaming. *Interface Focus.* 5:20150030.
46. Ellis, R. J. 2001. Macromolecular crowding: obvious but underappreciated. *Trends Biochem. Sci.* 26:597–604.
47. Hilitski, F., A. R. Ward, …, Z. Dogic. 2015. Measuring cohesion between macromolecular filaments one pair at a time: depletion-induced microtubule bundling. *Phys. Rev. Lett.* 114:138102.
48. Fisher, M. E., and D. Ruelle. 1966. The stability of many-particle systems. *J. Math. Phys.* 7:260–270.
49. Zacharias, M., T. P. Straatsma, and J. A. McCammon. 1994. Separation-shifted scaling, a new scaling method for Lennard-Jones interactions in thermodynamic integration. *J. Chem. Phys.* 100:9025–9031.
50. Abkenar, M., K. Marx, …, G. Gompper. 2013. Collective behavior of penetrable self-propelled rods in two dimensions. *Phys. Rev. E Stat. Nonlin. Soft Matter Phys.* 88:062314.
51. Kuan, H.-S., and M. D. Betterton. 2016. Motor protein accumulation on antiparallel microtubule overlaps. *Biophys. J.* 110:2034–2043.
52. Happel, J., and H. Brenner. 1983. Low Reynolds Number Hydrodynamics, Vol. 1. Martinus Nijhoff, The Hague, the Netherlands.
53. Tao, Y.-G., W. K. den Otter, …, W. J. Briels. 2005. Brownian dynamics simulations of the self- and collective rotational diffusion coefficients of rigid long thin rods. *J. Chem. Phys.* 122:244903.
54. Löwen, H. 1994. Brownian dynamics of hard spherocylinders. *Phys. Rev. E Stat. Phys. Plasmas Fluids Relat. Interdiscip. Topics.* 50: 1232–1242.
55. Giomi, L., M. J. Bowick, …, M. C. Marchetti. 2014. Defect dynamics in active nematics. *Phil. Trans. R. Soc. A.* 372:20130365.
56. Chen, J. Z. Y. 2013. Structure of two-dimensional rods confined by a line boundary. *Soft Matter.* 9:10921–10930.
57. Kruse, K., and F. Jülicher. 2000. Actively contracting bundles of polar filaments. *Phys. Rev. Lett.* 85:1778–1781.
58. Block, S. M., L. S. B. Goldstein, and B. J. Schnapp. 1990. Bead movement by single kinesin molecules studied with optical tweezers. *Nature.* 348:348–352.
59. Howard, J., A. J. Hudspeth, and R. D. Vale. 1989. Movement of microtubules by single kinesin molecules. *Nature.* 342:154–158.
60. Hackney, D. D. 1995. Highly processive microtubule-stimulated ATP hydrolysis by dimeric kinesin head domains. *Nature.* 377:448–450.
61. Howard, J. 2001. Mechanics of Motor Proteins and the Cytoskeleton. Sinauer Associates, Sunderland, MA.
62. Chrétien, D., and R. H. Wade. 1991. New data on the microtubule surface lattice. *Biol. Cell.* 71:161–174.
63. Wirtz, D. 2009. Particle-tracking microrheology of living cells: principles and applications. *Annu. Rev. Biophys.* 38:301–326.
64. Brady, S. T., K. K. Pfister, and G. S. Bloom. 1990. A monoclonal antibody against kinesin inhibits both anterograde and retrograde fast axonal transport in squid axoplasm. *Proc. Natl. Acad. Sci. USA.* 87:1061–1065.
65. Crevel, I., N. Carter, …, R. Cross. 1999. Coupled chemical and mechanical reaction steps in a processive *Neurospora* kinesin. *EMBO J.* 18:5863–5872.
66. Coppin, C. M., J. T. Finer, …, R. D. Vale. 1995. Measurement of the isometric force exerted by a single kinesin molecule. *Biophys. J.* 68 (*Suppl*):242S–244S.

Biophysical Journal, Volume *113*

Supplemental Information

Enhanced Dynamics of Confined Cytoskeletal Filaments Driven by Asymmetric Motors

Arvind Ravichandran, Gerrit A. Vliegenthart, Guglielmo Saggiorato, Thorsten Auth, and Gerhard Gompper

CONTENTS

S.I. Hybrid Brownian Dynamics 3
  A. Initial Condition 3
  B. Microtubules and Motors 3
  C. Iteration 4

S.II. Potentials 5
  A. Motors 5
  B. Inter-MT potential 5
  C. MT-wall interaction 8

S.III. Parameters 10
  A. Packing fraction 11
  B. Confinement diameter 12
  C. Motor concentration 12
  D. Motor spring constant 13
  E. Motor velocity 13

S.IV. Local Polar Order Parameter 20

S.V. Supplementary Figures 23

S.VI. Supplementary Videos 28

Supporting References 31

S.I. HYBRID BROWNIAN DYNAMICS

A. Initial Condition

The initial distribution of microtubules (MTs) is straightforward, because the inter-MT potential allows for overlap. First, we pick a random point within the circle defined by the confinement wall, which will potentially be the center of mass of a new MT. Next, we pick a random orientation, and check if the MT intersects with the confining wall. If it does not, we place the MT and proceed to placing the next MT until the necessary number of MTs are placed within the confinement. High overlap penalties tend to remove overlaps within a few thousand molecular dynamics steps, even at high densities.

B. Microtubules and Motors

There are two stochastic processes in our simulations. The first is the Gaussian distributed random displacements, $\delta \boldsymbol{r}_i(t)$, and rotations, $\delta \boldsymbol{p}_i(t)$ of MTs. This process is discussed in the main text. The second is the selection of the attachment position of the motor arms.

At each time step, the distances between beads on neighbouring MTs are checked. If the number of motors attached in the system is less than the predefined number of motors in the entire system, N_{m}, bead pairs that have inter-particle distance smaller than the threshold distance, d_{t}, are picked randomly, and motors are attached between them. The motors act as harmonic bonds with stiffness k_{m}, and energy, $U_{\mathrm{m}} = k_{\mathrm{m}} d^2/2$.

A motor arm that is attached to a MT walks with velocity v_{m} until the distance between the two motor arms reaches the stall length, d_{s}. For extensions beyond d_{s}, the motor arms stop walking. If the motor extension is larger than d_{t}, both arms of the motor detach simultaneously (Fig. S1).

Motion of the motor arms also depends on whether the motors are dimeric or tetrameric. Dimeric motors have one randomly picked anchored motor arm, which remains anchored to one MT until the motor extension is larger than d_{t}. The other motor arm walks on the MT with the velocity shown in Fig. S1, as do both arms of a tetrameric motor. We have no stochastic motor detachment rate, since kinesin molecules are known to be very processive [1].

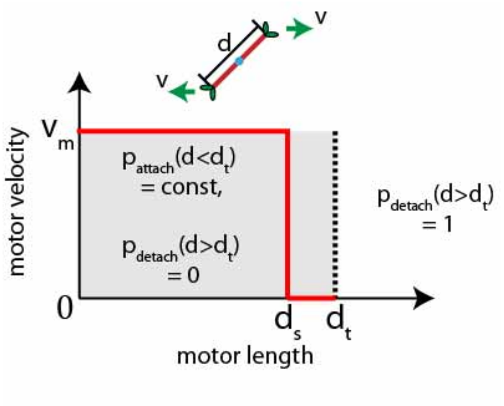

FIG. S1. Motors bind to neighbouring MTs with a constant probability if their length, d, is less than threshold distance, $d_{\rm t}$, until the predefined number of attached motors in the system, $N_{\rm m}$ is reached. Motors that are longer than $d_{\rm t}$ detach. If the motor length is less than the stall length, *i.e.* for $d < d_{\rm s}$, active motor arms move with constant velocity, $v_{\rm m}$.

C. Iteration

The overall Brownian dynamics scheme is:

1. Compute forces and torques due to MT attraction and repulsion.
2. If the number of attached motors is less than $N_{\rm m}$, look for beads on two different MTs which are closer than d_t, and attach motor arms to these MT pairs. If motors are active, *i.e.*, $d < d_{\rm s}$, displace each arm by $v_{\rm m}\delta t$ along the polar direction of the MT to which it is attached.
3. Calculate forces and torques on the MTs due to motors and confinement. Add these values to those obtained from 1.
4. Move MTs based on their respective forces and torques.
5. Update motor arm positions, such that the positions of the arms are conserved after step 4 on the MTs from before step 4. Remove the motors that are stretched beyond the motor threshold, *i.e.*, $d > d_{\rm t}$, and those motors that contain arms that have walked off the MT.

All the data collected from systems has been measured after the simulations have run for at least $1.5 \times 10^3\tau$, where τ is the onset of the activity time scale discussed in the main text.

S.II. POTENTIALS

MT dynamics occurs either because of forces from the motors, the inter-MT potential or the interaction between MTs and the wall.

A. Motors

Consider two MTs, i and j, each of length, L, with orientations $\boldsymbol{p}_i$ and $\boldsymbol{p}_j$, which correspond with the directions of motor arm motion, and center-of-masses $\boldsymbol{r}_i$ and $\boldsymbol{r}_j$. Note that orientation vectors $\boldsymbol{p}_i$ and $\boldsymbol{p}_j$ are necessarily unit vectors. They are parametrised by contour variables s_i and s_j that equal 0 and 1 at the negative and positive ends of the MTs respectively. A motor that crosslinks these MTs will have arms at positions $\boldsymbol{m}_i$ and $\boldsymbol{m}_j$ on MTs i and j respectively, with motor lengths $|\boldsymbol{m}_{ij}| = |\boldsymbol{m}_j - \boldsymbol{m}_i|$. We can write a motor arm position, $\boldsymbol{m}_i$ using,

$$\boldsymbol{m}_i = \boldsymbol{r}_i + L s_i \boldsymbol{p}_i. \tag{S1}$$

Since the motor is treated as a harmonic spring, the motor energy can be written as,

$$U_{\mathrm{m}} = \begin{cases} \frac{1}{2} k_{\mathrm{m}} |\boldsymbol{m}_{ij}|^2, & |\boldsymbol{m}_{ij}| \leq d_{\mathrm{t}} \\ 0, & |\boldsymbol{m}_{ij}| > d_{\mathrm{t}} \end{cases}, \tag{S2}$$

B. Inter-MT potential

MTs are simulated as rigid rods of length L and radius $r_{\min}$. They are composed of linearly arranged particles (beads). In order for MTs to "feel" each other as contiguous entities, and not a collection of discrete beads, the beads overlap. We placed a bead every $0.5r_{\min}$, such that $L = 0.5r_{\min}\left(N_{\mathrm{B}} - 1\right)$. Each bead which makes up an MT, interacts with beads from neighbouring MTs with a capped interaction potential, which has an attractive component. The general form of the potential used in our simulation is

$$U(r) = A_R \left(\frac{s^m}{r^m + \alpha^m} \right)^n - A_{\mathrm{A}} \left(\frac{s^m}{r^m + \alpha^m} \right)^{n/2} \tag{S3}$$

Here, α, A_{A} and A_{R} are dependent on overlap penalty, E_{R}, attraction energy, E_{A}, and the position of the attractive well, $r_{\min}$,

$$\alpha = r_{\min} \left(\left(1 + \sqrt{E_{\mathrm{R}}/E_{\mathrm{A}}} \right)^{2/n} - 1 \right)^{-1/m}, \tag{S4}$$

$$A_{\mathrm{A}} = 2\alpha^{mn/2} s^{-mn/2} E_{\mathrm{A}} \left(1 + \sqrt{E_{\mathrm{R}}/E_{\mathrm{A}}} \right), \tag{S5}$$

and

$$A_{\mathrm{R}} = \frac{A_{\mathrm{A}}^2}{4E_{\mathrm{A}}}. \tag{S6}$$

The variable s depends on the length of MTs, L, and the number of particles that makes up this MT, N_{B}:

$$s = \frac{L}{(N_{\mathrm{B}} - 1)}. \tag{S7}$$

For all simulations, $m = 2$, $n = 8$ and $r_{\min} = 1$. The exponents of the potential are chosen such that the superposition of multiple, overlapping beads gives a smooth, attractive MT-MT interaction, with a repulsive core. To characterise the potential, instead of looking at interaction energies between particles, we look at interaction energies between MTs in different orientations. In the following examples, one of the MTs (dark blue MT in Figs. S2, S3, S4) is fixed in position, and the position of the other MT is varied. We plot the energy that arises as a result of the superposition of the potentials between beads from the neighbouring MT.

Fig. S2 shows the energy of the two MTs as function of the separation distance, Δx for $E_{\mathrm{R}} = 6k_{\mathrm{B}}T$ and $E_{\mathrm{R}} = 20k_{\mathrm{B}}T$. We notice that the position of the minimum attraction energy shifts closer to the core of the MT than $r_{\min}$, because of the superposition of the energy wells of multiple beads. We will call this distance $x_{\min}$ and use it only for the MT sliding example discussed below. We use $E_{\mathrm{R}} = 20k_{\mathrm{B}}T$ for all calculations in the main text. At this level of repulsion, the overlap penalty is six fold higher than the energy of attraction, which makes MT crossings rare.

In order to ensure that A_{R} does not diverge, we take the limit $E_{\mathrm{A}} \to 0$ for curves marked $E_{\mathrm{A}} = 0.0$. Because of the manner in which our potential is constructed, the shape of the

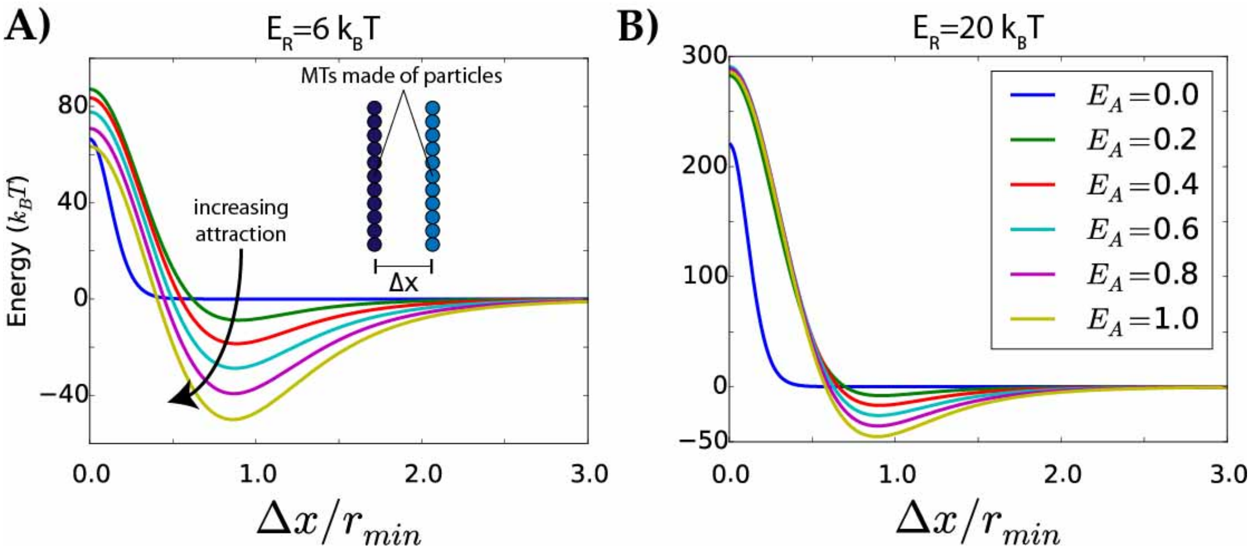

FIG. S2. Inter-MT energy as a function of separation distance, Δx, between an aligned MT pair, for different E_A values. Two regimes of repulsion are illustrated: (A) $E_\mathrm{R} = 6k_\mathrm{B}T$ and (B) $E_\mathrm{R} = 20k_\mathrm{B}T$. Negative energies indicate attraction, and positive energies indicate repulsion. Inset in (A) shows the orientation with which the calculation is conducted.

potential for $E_\mathrm{A} = 0$ differs substantially from larger values of E_A (Fig. S2). We, thus, do not use this potential to simulate systems which are not attractive.

Fig. S3 shows the energy of the MTs as a function of their parallel displacement, Δy. In this instance, we slide two aligned MTs apart, along their longitudinal axis. We keep the orthogonal displacement to be the position where the inter-MT energy is the smallest, $x_\mathrm{min} = 0.8r_\mathrm{min}$. The energy increases monotonically as the filaments slide away from each other, since the attractive interactions decrease, as the number of interacting beads decreases. When the centers of masses are separated further than the MT length, the number of interacting beads decreases to 1, and then the energy vanishes as the MTs are moved further away. The values chosen for the attraction energies correspond with the range of cohesion energies for the *in vitro* MT sliding experiment calculated for different PEG concentration [2].

In Fig. S3, two MTs are rotated with respect to each other, with the center beads of both MTs overlapping. For $E_\mathrm{R} = 6k_\mathrm{B}T$, and for $E_\mathrm{A} < 0.6k_\mathrm{B}T$ the potential is repulsive for all angles. For $E_\mathrm{R} = 6k_\mathrm{B}T$, $E_\mathrm{A} > 0.6k_\mathrm{B}T$, the potential has minima in two orientations. One must keep this in mind before using this potential for smaller overlap penalties, which can

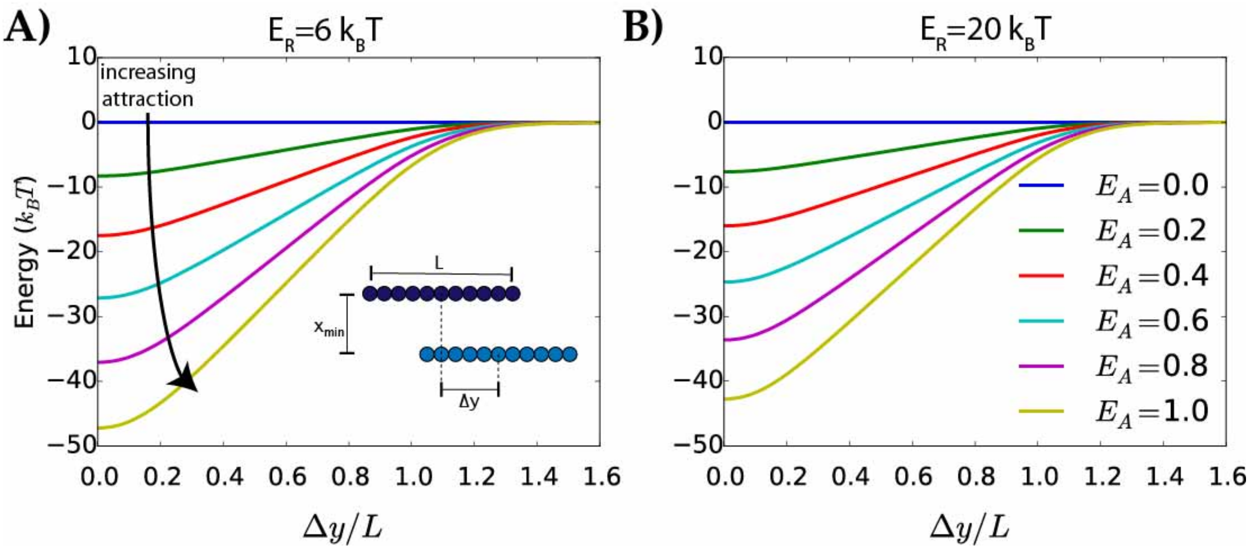

FIG. S3. Inter-MT energy as a function of parallel displacement between MTs' centers of masses, Δy, for different E_{A} values. The orthogonal displacement is set to be $x_{\min}$, the position of the energy well, seen in Figure S2. We illustrate two regimes of repulsion: (A) $E_{\mathrm{R}} = 6k_{\mathrm{B}}T$ and (B) $E_{\mathrm{R}} = 20k_{\mathrm{B}}T$. In both cases $x_{\min} = 0.8r_{\min}$. Inset in (A) shows the orientation with which the calculation is conducted.

lead to clustering of filaments due to such stable orientations. We avoid this issue here by using $E_{\mathrm{R}} = 20k_{\mathrm{B}}T$. This makes the potential repulsive for all values of E_{A}.

C. MT-wall interaction

Self-propelled, active particles are known to accumulate at confinement walls [3]. In order to stabilise a layer of MTs close to the wall, in our work, we adhere MTs to the wall using an attractive wall potential. Beads which make up the MTs interact with the wall with a 6-12 Lennard Jones potential,

$$U_{\mathrm{w}}(r) = \begin{cases} 4\epsilon \left[\left(\frac{r_{\min}}{r}\right)^{12} - \left(\frac{r_{\min}}{r}\right)^{6} \right] & r \leqslant 3r_{\min} \\ 0 & r > 3r_{\min} \end{cases}, \tag{S8}$$

where r is the distance between a bead and the wall, and $r_{\min}$ is the position of the attractive energy well. We choose the same range, $3r_{\min}$, for MT-MT interactions and MT-wall interactions. Superposition of these potentials between all the beads that make up an MT

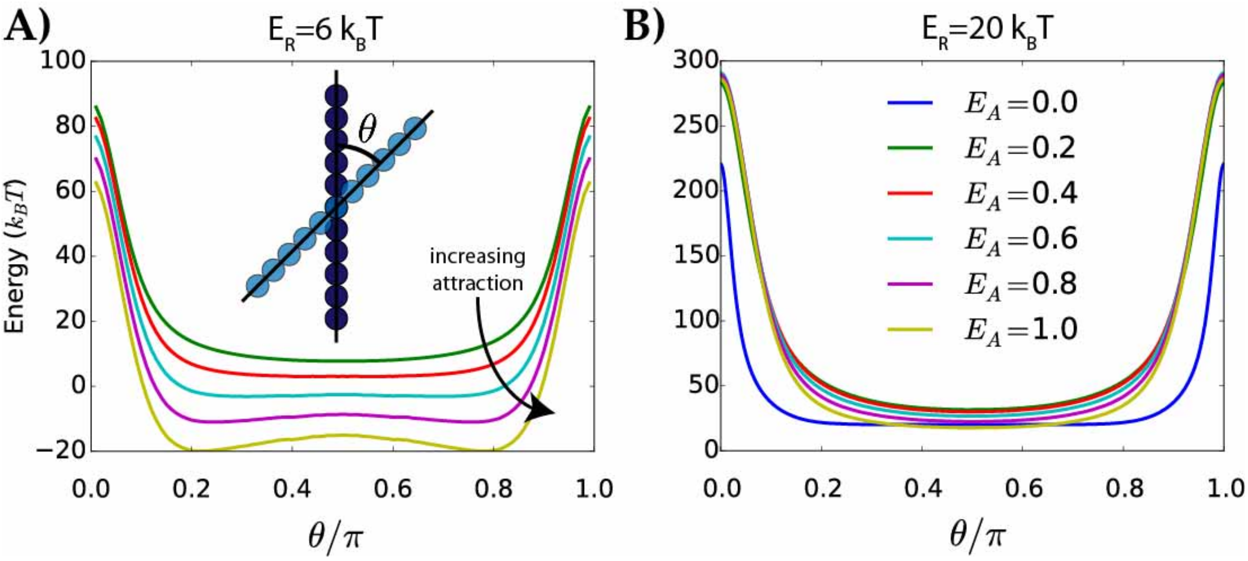

FIG. S4. Inter-filament energy as a function of increasing the angle of crossing between two overlapping filaments, θ, for different E_A values. We illustrate two regimes of repulsion: (A) $E_\mathrm{R} = 6k_\mathrm{B}T$ and (B) $E_\mathrm{R} = 20k_\mathrm{B}T$. Inset in (A) shows the orientation with which the calculation is conducted.

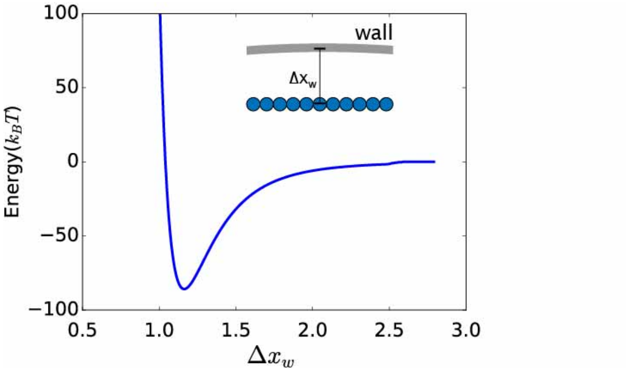

FIG. S5. Interaction energy of MT with the wall with a 6-12 Lennard Jones potential. $\epsilon_\mathrm{w} = 8k_\mathrm{B}T$, $\sigma_\mathrm{w} = r_\mathrm{min}$. Δx_w are given in units of r_min.

and the wall gives the curve shown in Fig. S5.

A comparison of the energies in Fig. S5, with those of Figs. S2, S3 and S4, shows that the attractive MT-wall interaction energy is sufficient to stabilise a layer of partially overlapping MTs close to the wall [4], because the level of attraction is larger ($-90\ k_\mathrm{B}T$) than the other energies (attractive or repulsive) involved in the system.

S.III. PARAMETERS

The primary parameters varied in the simulations are attraction energy, E_{A}, and number of motors, N_{m}. Despite having taken a step toward capturing cellular scale phenomena by marrying three distinct components of very different length scales, we have tried to capture biologically accurate lengths in the simulation (Table S1). However, in our coarse-grained model we chose constant motor speeds, 3.6 times faster than motor speeds from single molecule experiments. In so doing we remove the force dependency on motor speed and shift the focus from the loads on individual motors to conduct MT sliding. Instead, we use motors as coarse-grained entities that propel MTs based on the MT pair's orientation. In order to traverse another order of magnitude in length scale and simulate MTs in cell-sized confinements, such coarse-graining choices need to be explored.

A complete list of parameters used in our simulations is given in Table S1. We match the parameters to biological values when possible. Note that the viscosity, η, is linked to the friction coefficient, γ_0, used in the dynamical equations [5].

We choose the MT diameter (r_{min}) and activity time scale (τ) as the characterstic length and time units, for defining dimensionless parameters, respectively. The thermal energy, $k_{\mathrm{B}}T$, is the characterstic energy scale. The dimensionless form of the parameters are collected in Table S2.

The results of a systematic study of the effect of the various parameters on the global structure and dynamics of MTs for both tetrameric and dimeric motor systems are summarised below. This concerns, in particular, the effect of varying area fraction, confinement size, motor concentration, motor spring constant and motor velocity.

Each MT is composed of 11 overlapping beads. For all the cases shown in the main text, there are 927 MTs within the confinement. If we define the MT diameter to be r_{min}, then the MTs have an aspect ratio of 5. In order to determine the area fraction of penetrable MTs within the confinement, we consider the effective bead radius to be $r_{\mathrm{eff}} = 0.8 r_{\mathrm{min}}$ (Fig. S21). For 927 MTs, the effective packing fraction of MTs is given by $N_{\mathrm{f}} r_{\mathrm{eff}} L / \pi R_{\mathrm{W}}^2 = 0.74$.

TABLE S1. Simulation Parameters

Parameter	Symbol	Value	Notes/Biological Values
Thermal energy	$k_{\mathrm{B}}T$	4.11 pN nm	Room Temperature
MT length	L	0.125 μm	2.5 ± 1.4 μm [6]
MT diameter	r_{min}	25 nm	25 nm [7]
Confinement radius	R_{W}	1 μm	Oocyte $\sim 200 \mu$m [4]
Repulsive peak	E_{R}	$20 k_B T$	Chosen
MT Attractive well	E_{A}	$0.2 - 1.0 k_{\mathrm{B}}T$	*in vitro* experiments [2]
Confining wall attraction	ϵ_{w}	$8.0 k_B T$	Chosen
Confining wall range	σ_{w}	25 nm	Chosen
Fluid viscosity	η	1 Pa s	Cytoplasmic viscosity [8]
Maximum motor speed	v_{m}	6.5 μm/s	Single motor speed ~ 1.8 μm/s [9]
Maximum motor extension	d_{t}	25 nm	80 nm [10]
Motor stall force	f_{s}	7.83 pN	5 pN [11]
Motor spring constant	k_{m}	0.33 pN/nm	Single kinesin molecule [12]

A. Packing fraction

To understand the effect of packing fraction on large scale structures, for both cases of motors, we performed simulations for 649, 834, 927, 1020, and 1205 MTs. The structures for these packing fractions are shown in Fig. S6. With increasing area fraction of MTs polarity sorting becomes more prominent, and polar aligned, structured domains become more pronounced for both types of motors. The diffusion of MTs are hindered for larger densities for lag times less than τ, for both motor models. This is clear when we compare the dynamics of motor-driven systems at higher densities with the passive system at an area fraction of 0.74. However, we observed similar levels of activity for dimeric motors, across all densities, for lag times larger than τ. For tetrameric motors, denser systems leads to

TABLE S2. Dimensionless Groups

Parameter	Symbol	Value
Area fraction	$\frac{N_\mathrm{f} r_\mathrm{eff} L}{\pi R_\mathrm{W}^2}$	0.74
MT aspect ratio	$\frac{L}{r_\mathrm{min}}$	5
Confinement diameter	$\frac{R_\mathrm{W}}{r_\mathrm{min}}$	80
Motor to MT ratio	$\frac{N_\mathrm{m}}{N_\mathrm{f}}$	1
Maximum motor speed	$\frac{v_\mathrm{m} \tau}{r_\mathrm{min}}$	50
Maximum motor extension	$\frac{d_\mathrm{t}}{r_\mathrm{min}}$	1
Motor stall force	$\frac{f_\mathrm{s} r_\mathrm{min}}{k_\mathrm{B} T}$	47.7
Motor spring constant	$\frac{k_\mathrm{m} d_\mathrm{t}}{f_\mathrm{s}}$	1

lower levels of activity across all lag times (Fig. S7).

B. Confinement diameter

Simulations of five different confinement diameters show an increase in the number of polar aligned domains with increasing confinement size for both the dimeric and tetrameric motor systems (Fig. S8). The active displacements increase with increasing confinement diameter for both motor systems, at large lag times, (Lag time/τ) $\geq 10^2$ (Fig. S9). As discussed in the main text, the MSD of MTs plateaus at the confinement radius. We observe larger active displacements for larger confinements, because MTs are not yet hindered by the confinement at this time scale.

C. Motor concentration

Motor concentration has the strongest effect on the structures observed, and is one of the primary parameters discussed in the main text. It is also a parameter that is accessible in experiments. At low motor concentrations, $N_\mathrm{m}/N_\mathrm{f} = 0.5$, the polarity sorting results in large polar-aligned domains for both dimeric and tetrameric motors, and there are not enough motors to induce large-scale motion. For $N_\mathrm{m}/N_\mathrm{f} = 3$, there is a higher proportion of MTs which are aligned with the confining wall for the dimeric motor system. Higher motor concentration further emphasises the bundling of MTs in the tetrameric motor system (Fig. S11).

Activity increases with increasing motor concentrations, because there are more active elements to slide MTs. However, this is more prominent in the dimeric motors than in the tetrameric motor system (Fig. S11). For dimeric motors, we show the onset of a plateau in the MSD upon reaching R_W^2, where a significant proportion of MTs' displacements are limited by the confining wall (Fig. S11C). On this time scale, we do not observe this for the tetrameric motors, because their dynamics is slower (Fig. S11D).

D. Motor spring constant

Increasing motor spring strength does not induce any appreciable change in overall structure of the system for both motor systems (Fig. S12). However, increasing the motor spring constant increases active displacements of MTs for both dimeric and tetrameric motor systems. This is the most effective method to diminish the difference in MT activity between the dimeric and tetrameric motors (Fig. S13).

E. Motor velocity

Increasing motor velocity does not change the overall structure of the system for both motor systems (Fig. S14). However, it decreases the crossover time between diffusion and activity dramatically for the dimeric motor system (Fig. S15). The differences between the tetrameric and dimeric motors are greatly enhanced for higher motor velocities, since the crossover time appears to be conserved for the tetrameric motors, possibly due to the lack of antialigned MTs. In the main text, we have used the motor velocity that is biologically motivated.

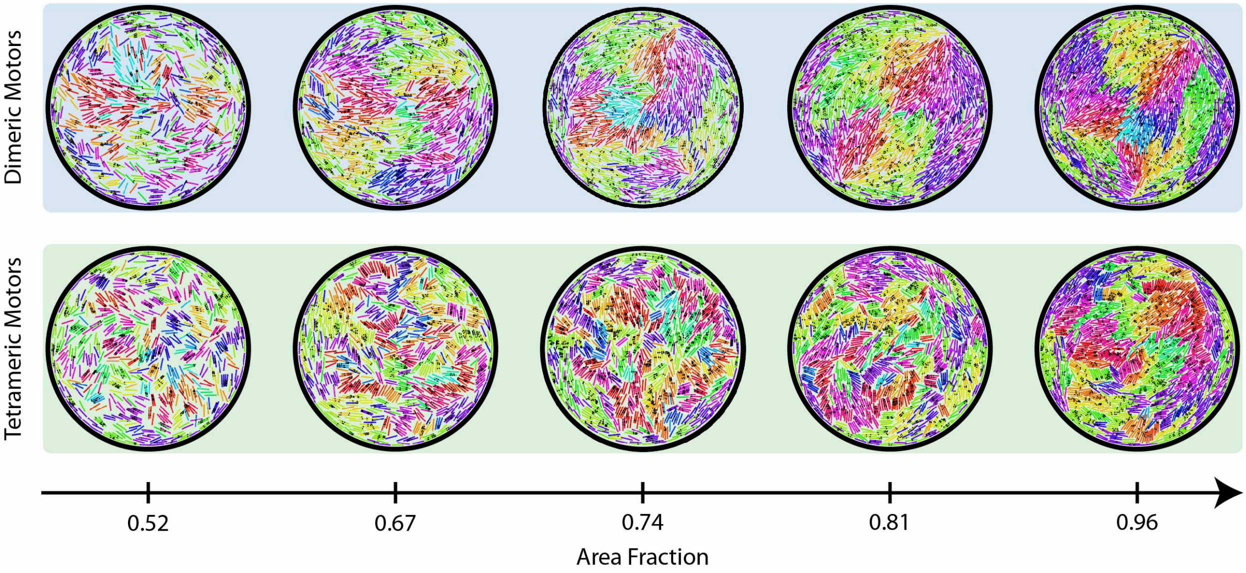

FIG. S6. Snapshots of steady state structures for different area fractions for dimeric and tetrameric motors. The area fractions correspond to 649, 834, 927, 1020, and 1205 MTs within the confinement. All packing fraction are computed using $r_{\text{eff}} = 0.8 r_{\text{min}}$. 927 MTs are used for all results in the main text. For these simulations, $R_{\text{W}}/L = 8$, $\epsilon_{\text{w}} = 8 k_{\text{B}} T$, $E_{\text{A}} = 0.2$, $v_{\text{m}} \tau / r_{\text{min}} = 50$, $k_{\text{m}} d_{\text{t}} / f_{\text{s}} = 1$ and $N_{\text{m}}/N_{\text{f}} = 1$.

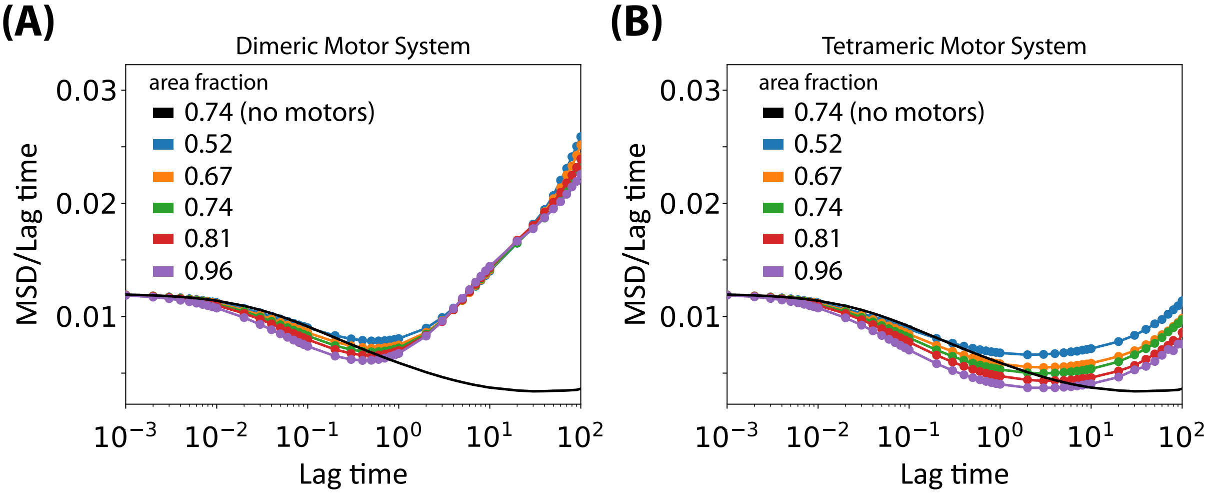

FIG. S7. MSD/Lag time for different area fractions for dimeric and tetrameric motors. The area fractions correspond to 649, 834, 927, 1020, and 1205 MTs within the confinement. MSD is normalised by L^2 and lag time is normalised by τ. $R_{\text{W}}/L = 8$, $\epsilon_{\text{w}} = 8 k_{\text{B}} T$, $E_{\text{A}} = 0.2 k_{\text{B}} T$, $v_{\text{m}} \tau / r_{\text{min}} = 50$, $k_{\text{m}} d_{\text{t}} / f_{\text{s}} = 1$ and $N_{\text{m}}/N_{\text{f}} = 1$.

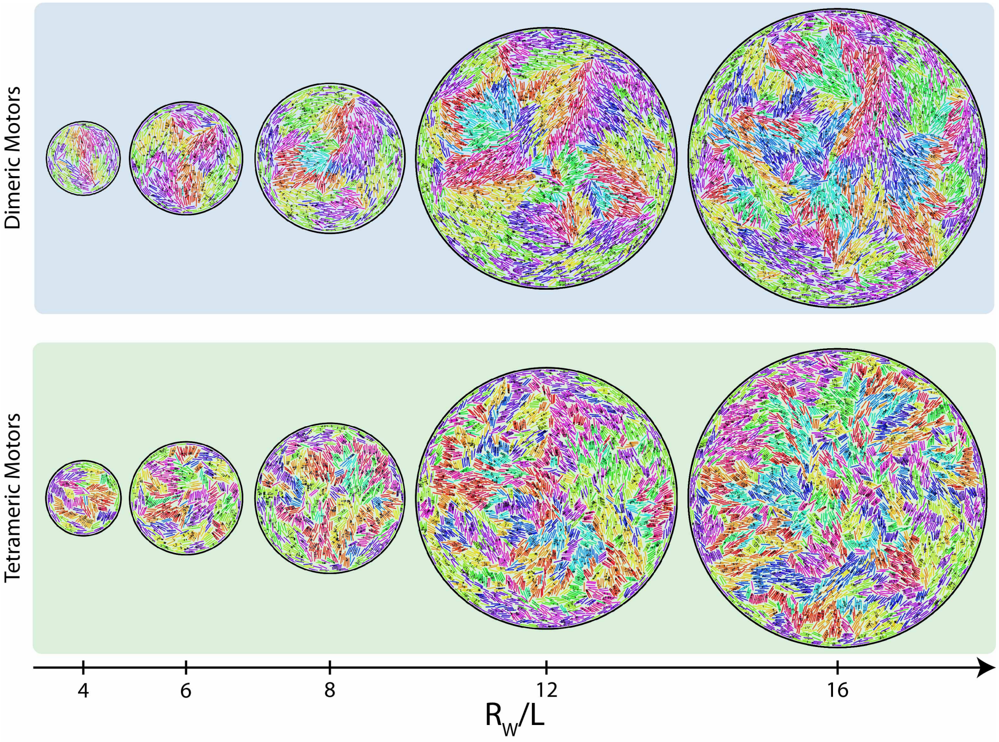

FIG. S8. Snapshots of steady state structures for different diameters of confinement relative to $r_{\rm min}$. We use $R_{\rm W}/L = 8$ for all findings in the main text. The area fraction is kept constant at 0.74, $\epsilon_{\rm w} = 8k_{\rm B}T$, $E_{\rm A} = 0.2k_{\rm B}T$, $k_{\rm m}d_{\rm t}/f_{\rm s} = 1$, $v_{\rm m}\tau/r_{\rm min} = 50$ and $N_{\rm m}/N_{\rm f} = 1$.

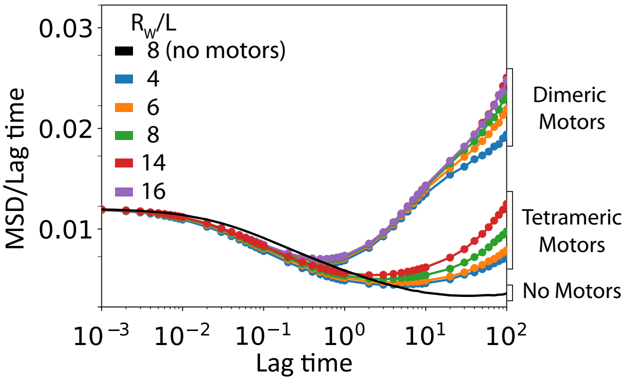

FIG. S9. MSD/Lag time for different confinement diameters. MSD is normalised by L^2 and lag time is normalised by τ. The area fraction is kept constant at 0.74, $\epsilon_{\rm w} = 8k_{\rm B}T$, $E_{\rm A} = 0.2k_{\rm B}T$, $k_{\rm m}d_{\rm t}/f_{\rm s} = 1$, $v_{\rm m}\tau/r_{\rm min} = 50$ and $N_{\rm m}/N_{\rm f} = 1$. Note that we use more MTs and more motors in systems with larger confinements.

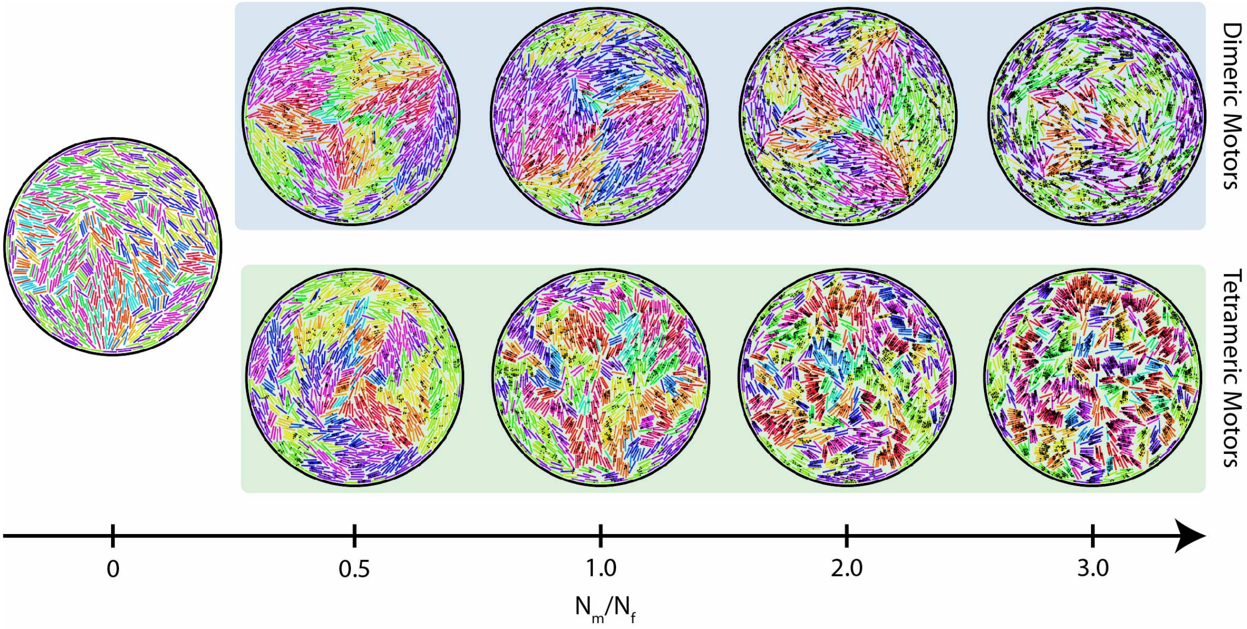

FIG. S10. Snapshots of steady state structures for different $N_\mathrm{m}/N_\mathrm{f}$ for dimeric and tetrameric motors. We use $N_\mathrm{m}/N_\mathrm{f} = 1$ for all findings in the main text. The area fraction is 0.74, $R_\mathrm{W}/L = 8$, $\epsilon_\mathrm{w} = 8k_\mathrm{B}T$, $E_\mathrm{A} = 0.2k_\mathrm{B}T$, $k_\mathrm{m}d_\mathrm{t}/f_\mathrm{s} = 1$ and $v_\mathrm{m}\tau/r_\mathrm{min} = 50$.

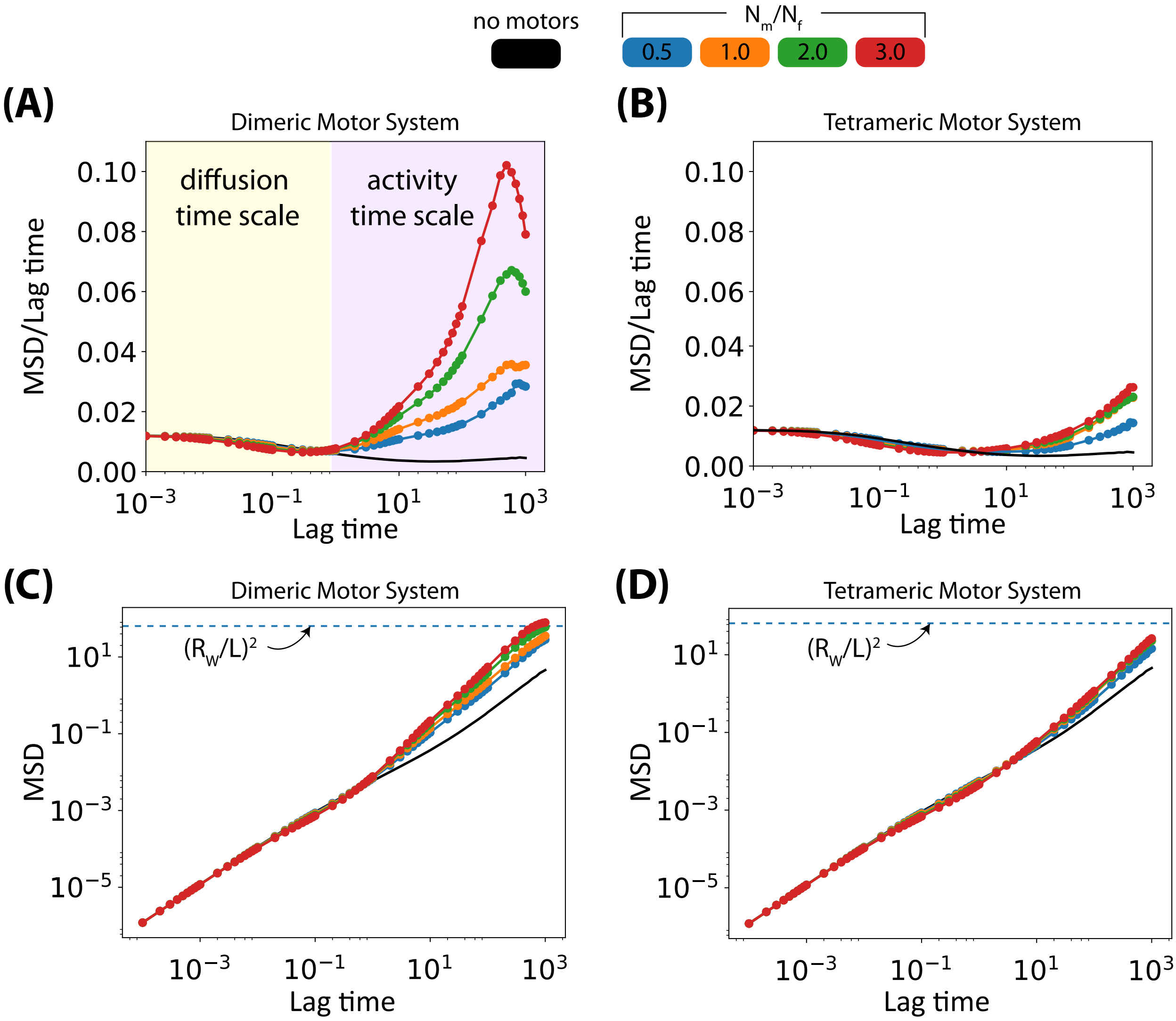

FIG. S11. MSD/Lag time for different $N_\mathrm{m}/N_\mathrm{f}$ for dimeric (A) and tetrameric (B) motors. MSD vs lag times for dimeric (C) and tetrameric (D) motors. The squared wall radius is represented by the dotted blue line in (C) and (D). MSD is normalised by L^2 and lag time is normalised by τ. The area fraction is 0.74, $R_\mathrm{W}/L = 8$, $\epsilon_\mathrm{w} = 8k_\mathrm{B}T$, $E_\mathrm{A} = 0.2k_\mathrm{B}T$, $k_\mathrm{m}d_\mathrm{t}/f_\mathrm{s} = 1$ and $v_\mathrm{m}\tau/r_\mathrm{min} = 50$.

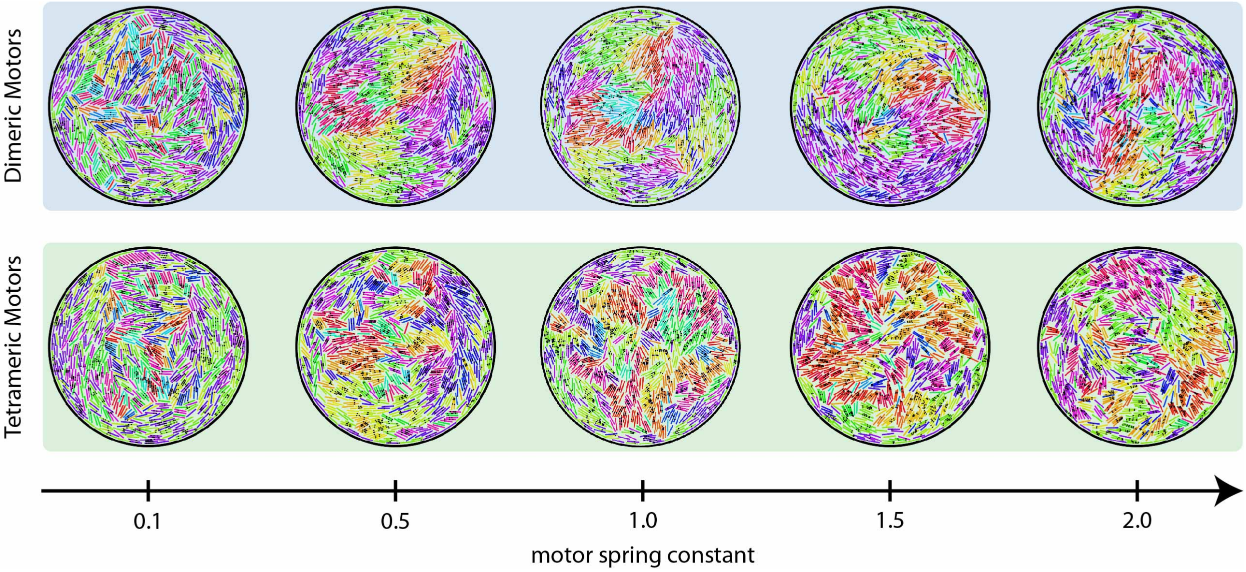

FIG. S12. Snapshots of steady state structures for different $k_\mathrm{m}d_\mathrm{t}/f_\mathrm{s}$. A motor spring constant of $k_\mathrm{m}d_\mathrm{t}/f_\mathrm{s} = 1$ was used for all findings in the main text. The area fraction is 0.74, $R_\mathrm{W}/L = 8$, $\epsilon_\mathrm{w} = 8k_\mathrm{B}T$, $E_\mathrm{A} = 0.2k_\mathrm{B}T$, $k_\mathrm{m}d_\mathrm{t}/f_\mathrm{s} = 1$, $v_\mathrm{m}\tau/r_\mathrm{min} = 50$ and $N_\mathrm{m}/N_\mathrm{f} = 1$.

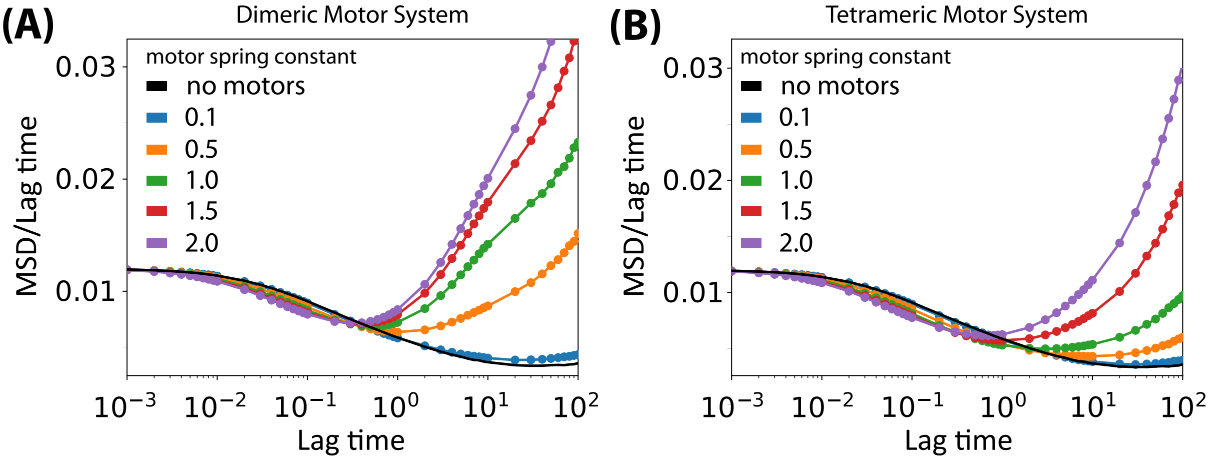

FIG. S13. MSD/Lag time for different $k_\mathrm{m}d_\mathrm{t}/f_\mathrm{s}$. MSD is normalised by L^2 and lag time is normalised by τ. The area fraction is 0.74, $\epsilon_\mathrm{w} = 8k_\mathrm{B}T$, $E_\mathrm{A} = 0.2k_\mathrm{B}T$, $v_\mathrm{m}\tau/r_\mathrm{min} = 50$, $R_\mathrm{W}/L = 8$ and $N_\mathrm{m}/N_\mathrm{f} = 1$.

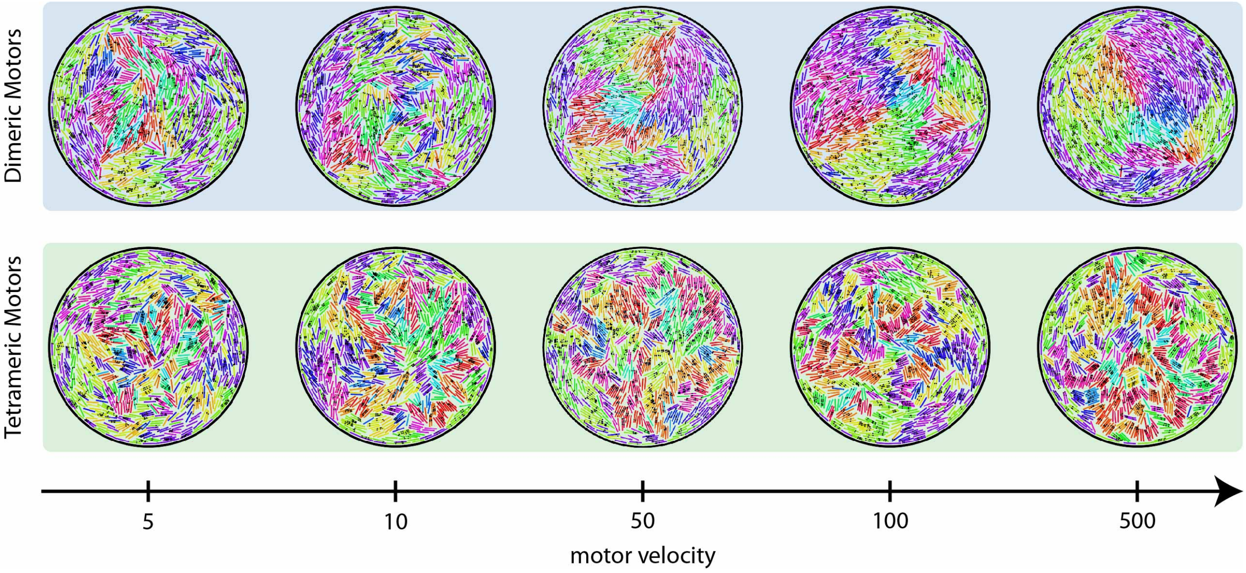

FIG. S14. Snapshots of steady state structures for different $v_{\mathrm{m}}\tau/r_{\mathrm{min}}$. A motor velocity of $v_{\mathrm{m}}\tau/r_{\mathrm{min}} = 50$ was used for all findings in the main text. The area fraction is 0.74, $R_{\mathrm{W}}/L = 8$, $\epsilon_{\mathrm{w}} = 8k_{\mathrm{B}}T$, $E_{\mathrm{A}} = 0.2k_{\mathrm{B}}T$, $k_{\mathrm{m}}d_{\mathrm{t}}/f_{\mathrm{s}} = 1$ and $N_{\mathrm{m}}/N_{\mathrm{f}} = 1$.

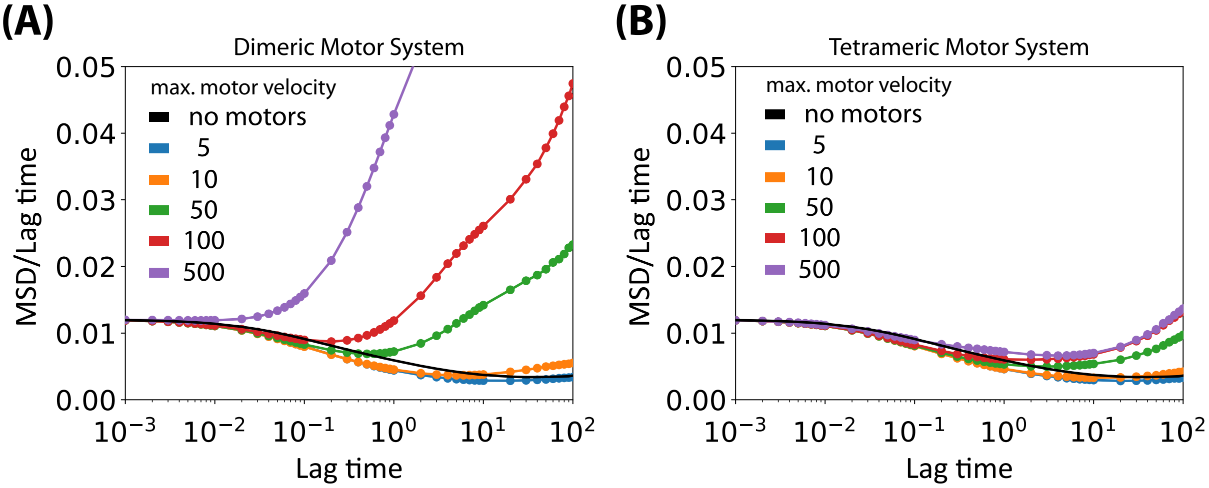

FIG. S15. MSD/Lag time for different $v_{\mathrm{m}}\tau/r_{\mathrm{min}}$. MSD is normalised by L^2 and lag time is normalised by τ. The area fraction is 0.74, $R_{\mathrm{W}}/L = 8$, $\epsilon_{\mathrm{w}} = 8k_{\mathrm{B}}T$, $E_{\mathrm{A}} = 0.2k_{\mathrm{B}}T$, $k_{\mathrm{m}}d_{\mathrm{t}}/f_{\mathrm{s}} = 1$ and $N_{\mathrm{m}}/N_{\mathrm{f}} = 1$.

S.IV. LOCAL POLAR ORDER PARAMETER

In order to characterise a MT's neighbourhood, we define a pairwise motor partition function, $q_{ij}(\boldsymbol{r}_i, \hat{\boldsymbol{p}}_i, \boldsymbol{r}_j, \hat{\boldsymbol{p}}_j)$ as [13]

$$q_{ij} = \rho^2 \int_{-1/2}^{1/2} ds_i \int_{-1/2}^{1/2} ds_j e^{-\beta U_{\mathrm{m}}(|\boldsymbol{m}_{ij}|)}, \tag{S9}$$

where ρ is the linear density of binding sites on a single MT, and s_i and s_j parametrise the positions of motor arms on MTs i and j, respectively (Eq. S1).

The quantity weights pairwise interactions of MTs on the basis of motor binding site availability, which is a function of MT pair's relative orientation and distance. For instance, q_{ij} becomes significant only for pairs of MTs in close proximity, and $q_{ij} = 1$ when they are perfectly overlapping each other. When two MTs are sufficiently far away, such that no motors can interact between them, $q_{ij} = 0$, and the MTs are said to be outside motor range (Fig. S16(A and E)). Since the motor energy $U_{\mathrm{m}}(|\boldsymbol{m}_{ij}|)$ increases quadratically with increasing motor extension (Eq. S2), the partition function, q_{ij}, decays rapidly as binding sites for motors on the MTs become farther and less (Figure S16).

For MTs within motor range, we define them to be antialigned if $(\boldsymbol{p}_i \cdot \boldsymbol{p}_j) < 0$ and polar-aligned if $(\boldsymbol{p}_i \cdot \boldsymbol{p}_j) \geq 0$. Weighing $(\boldsymbol{p}_i \cdot \boldsymbol{p}_j)$ by q_{ij} gives a good representation of local polar order, because it invokes the polarity of just the neighbourhood of the MT in question. And the notion of neighbourhood is clearly defined as the availability of motor binding between the MT pair in question. Moreover, by taking the sum of all interacting MTs with MT i, $\psi(i) = \sum_{i \neq j} (\boldsymbol{p}_i \cdot \boldsymbol{p}_j) q_{ij} / \sum_{j \neq i} q_{ij}$, depends solely on the polarity of the neighbourhood of MT i. We employ $\psi(i)$ to find correlations in velocities with the polarity of MT neighbourhood.

Figure S17 shows antiparallel and parallel orientations of MTs at stationary state for systems with dimeric and tetrameric motors, where MTs are coloured based on their local polar order parameter. In the dimeric motor system (Fig. S17A), large polar-aligned MT clusters compose the entire system. Geometric frustration due to the confinement, and the motion of MTs within polar-aligned clusters give rise to an interface of antialigned MTs that is perpetually created and destroyed throughout the simulation. A significant population of motile, antialigned MTs are observed, in particular close to the confining wall. For the system with tetrameric motors (Fig. S17B), static, polar-aligned bundles of strongly attracting MTs make up the system. The strong attraction within aligned bundles hinders the for-

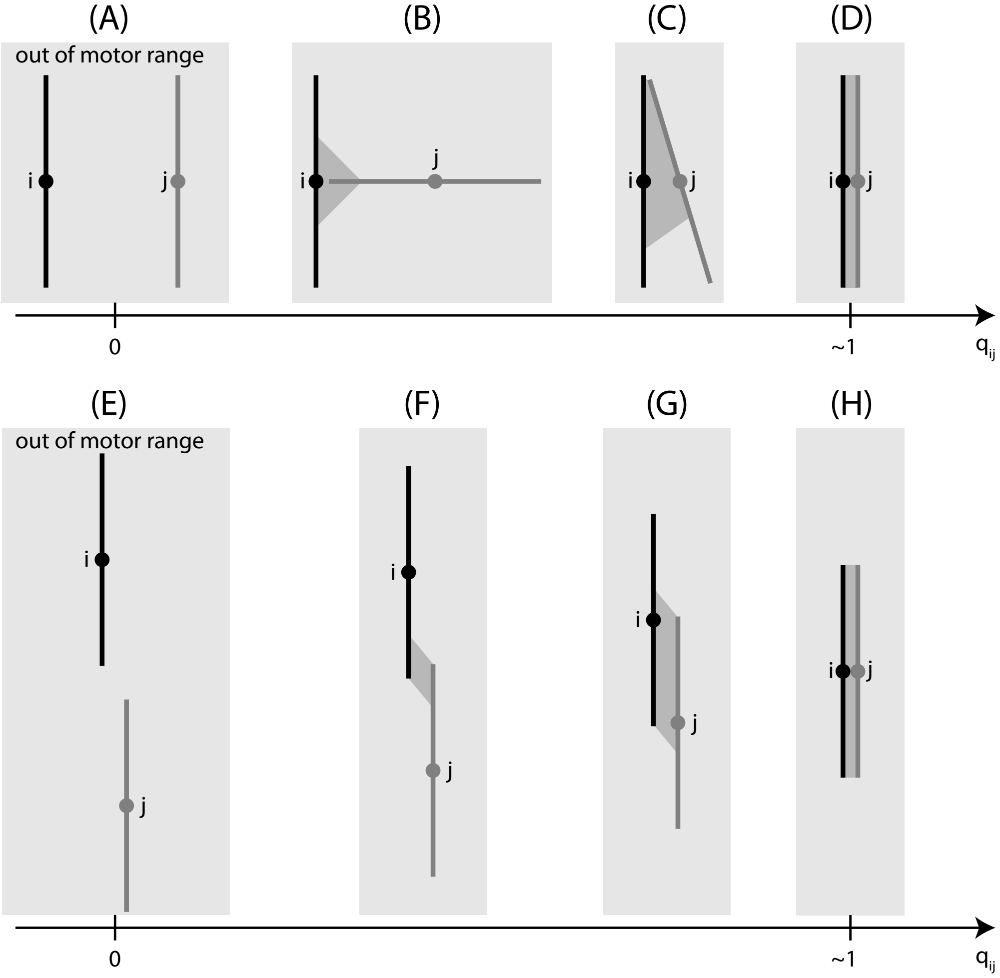

FIG. S16. Pairwise motor partition function, q_{ij}, quantifies the availability of motor binding between MT pairs. (A, B, C and D) shows the effect of rotational degrees of freedom on MT pairs. (E, F, G, H) shows the effect of translational degrees of freedom on MT pairs. The shaded region indicates the region available for motor binding. (D) and (H) are identical and show an instance of near perfect overlap, and availability of motor binding between MT pairs.

mation of interfaces of antialigned MTs. Nevertheless, the confinement hinders the sorting mechanism, such that a considerable population of antialigned MTs is observed. They appear intermittently, and quickly become members of polar-aligned bundles, re-establishing the stationary structure of the system.

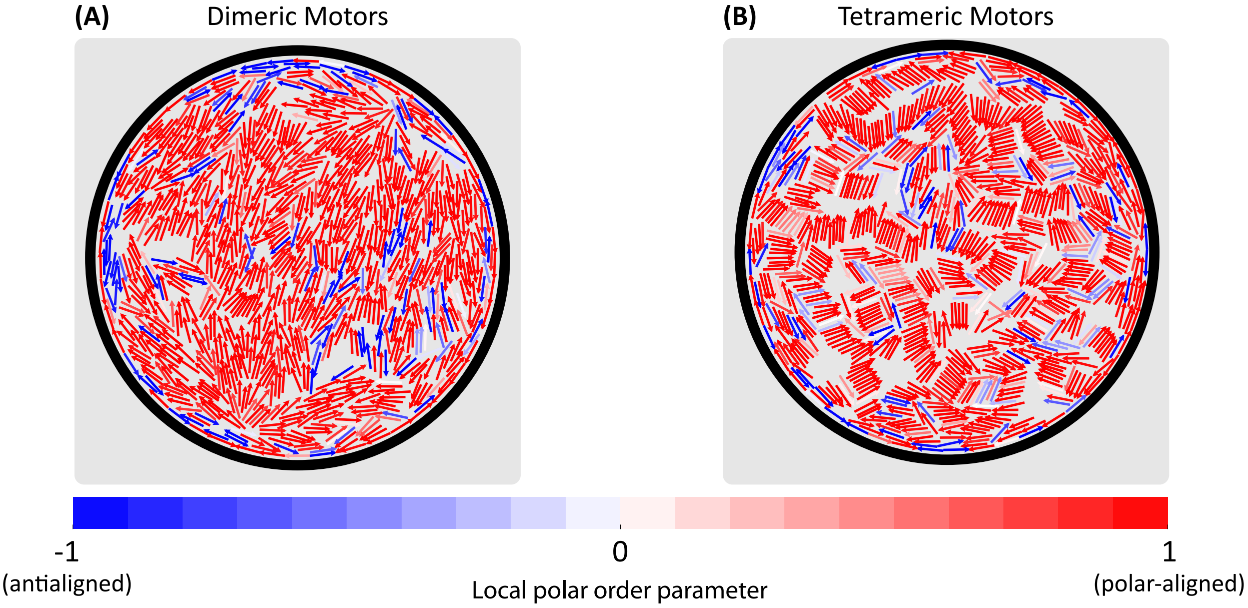

FIG. S17. Stationary configuration of MTs in systems with (A) dimeric and (B) tetrameric motors for $E_A = 1.0 k_B T$ and $N_m/N_f = 1$. Arrow heads represent the direction of motor-arm motion on MT. The colour of each arrow represents the local polar orientational order parameter.

S.V. SUPPLEMENTARY FIGURES

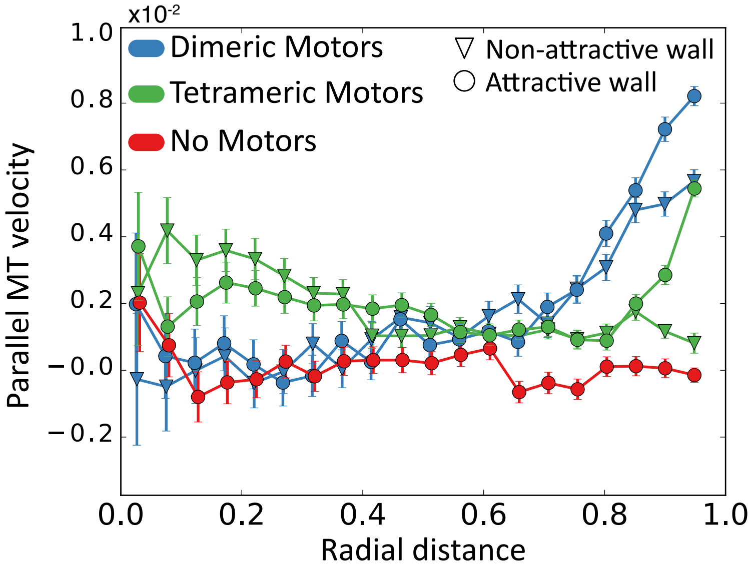

FIG. S18. Parallel MT velocity vs. radial distance for tetrameric, dimeric and passive systems. This is the same as Fig. 9 in the main text, but includes the velocities for the cases with both attractive and non-attractive confining walls. MTs near the confining wall are slower in the systems with the non-attractive walls relative to the systems with the attractive wall. $E_{\mathrm{A}} = 0.2k_{\mathrm{B}}T$ and $N_{\mathrm{m}}/N_{\mathrm{f}} = 1$. Velocities are normalised by L/τ. Radial distance is normalised by confining wall radius, R_{W}.

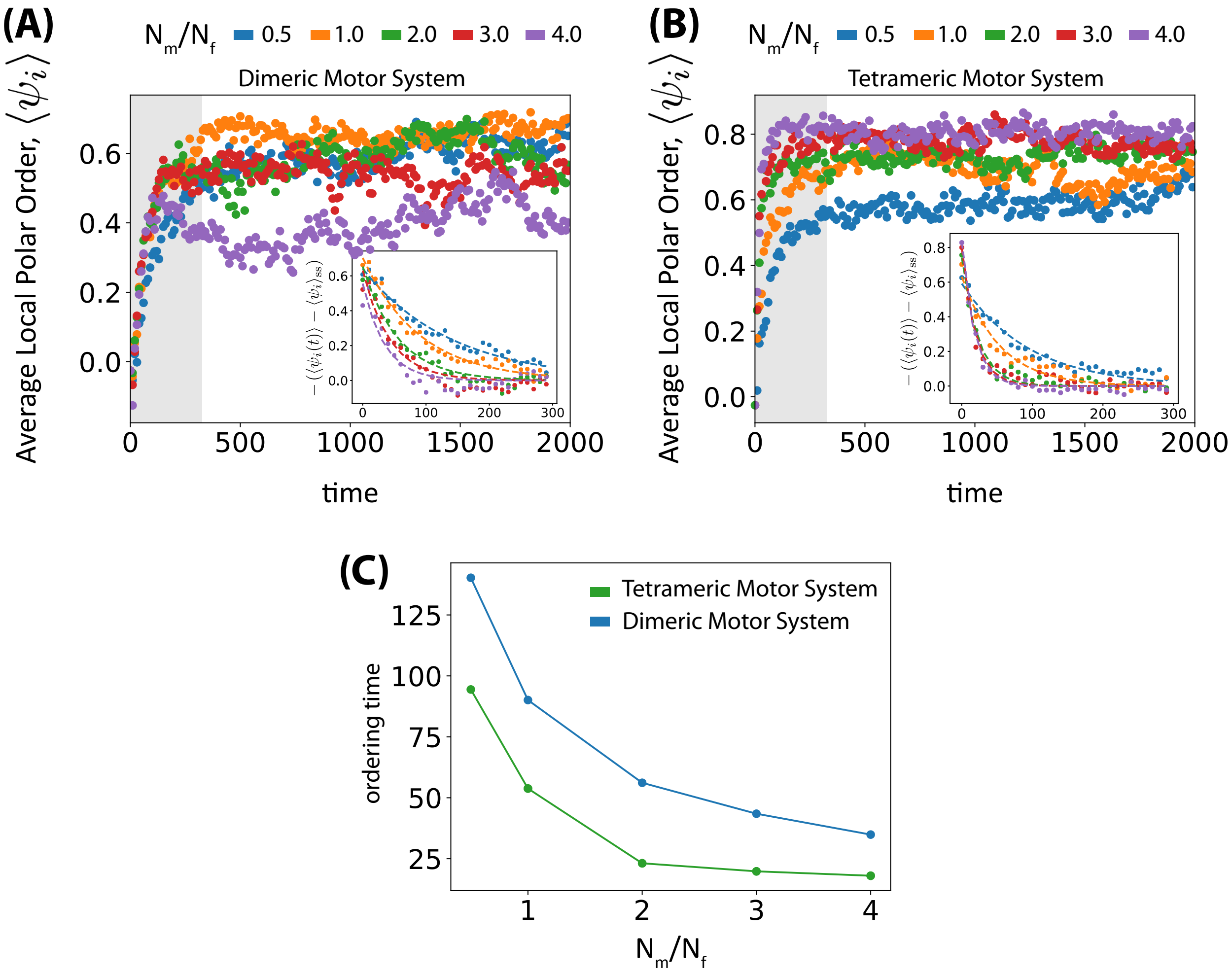

FIG. S19. Estimation of time taken to form structures for dimeric and tetrameric motor systems for different motor concentrations. The system evolves from the initial state of an equilibrated no motor system. The average local polar order $\langle \psi_i \rangle$ is the mean ψ_i of all MTs in the system at a given time. This is seen to fluctuate about a fixed value for both dimeric (A) and tetrameric (B) motor systems. Assuming that the ordering only happens initially, we fit a decaying exponential, $A\exp(-t/\lambda)$ to this data, $-(\langle \psi_i(t) \rangle - \langle \psi_i \rangle_{\mathrm{ss}})$ (insets). $\langle \psi_i \rangle_{\mathrm{ss}}$ is the steady state, average local polar order obtained from the last 1000 steps. (C) λ is reported as the ordering time as a function of different motor concentrations. Ordering time is normalised by, τ, the timescale for the onset of activity. Area fraction is 0.74, $R_{\mathrm{W}}/r_{\mathrm{min}} = 80$, $\epsilon_{\mathrm{w}} = 8k_{\mathrm{B}}T$, $E_{\mathrm{A}} = 0.2k_{\mathrm{B}}T$, $v_{\mathrm{m}}\tau/r_{\mathrm{min}} = 50$ and $k_{\mathrm{m}}d_{\mathrm{t}}/f_{\mathrm{s}} = 1$, as per simulations presented in the main text.

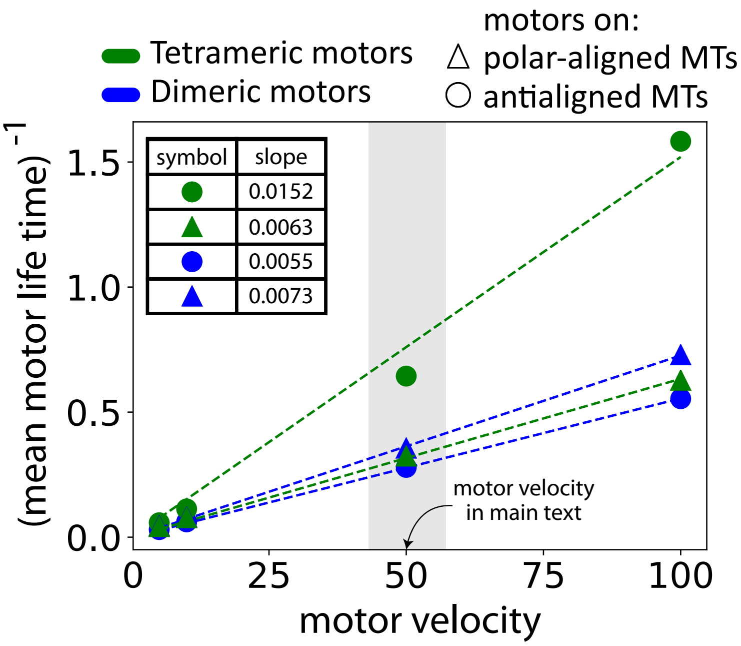

FIG. S20. Inverse of mean motor life time as a function of motor velocity for tetrameric and dimeric motors. Mean motor life time is obtained by fitting an exponential function, $A \exp(-t_{\mathrm{mp}}/\lambda_{\mathrm{mp}})$ to the histogram of motor processivity. t_{mp} and λ_{mp} is the motor processivity and the fitting parameter to obtain mean motor life time respectively. Mean motor life time is measured in units of τ. $\lambda_{\mathrm{mp}}^{-1}$ is plotted against motor velocity, and we report the slopes of linear fits in the table. We treat motors on polar-aligned MTs and antialigned MTs separately. Motor velocity is given as $v_{\mathrm{m}}\tau/r_{\mathrm{min}}$. Area fraction is 0.74, $R_{\mathrm{W}}/r_{\mathrm{min}} = 80$, $\epsilon_{\mathrm{w}} = 8k_{\mathrm{B}}T$, $E_{\mathrm{A}} = 0.2k_{\mathrm{B}}T$, $N_m/N_f = 1$ and $k_{\mathrm{m}}d_{\mathrm{t}}/f_{\mathrm{s}} = 1$.

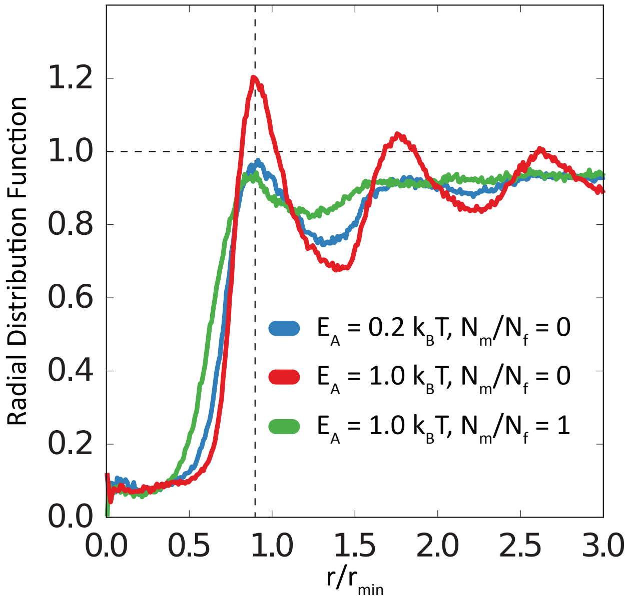

FIG. S21. Time-averaged radial distribution function of beads that make up MTs. We used dimeric motors for the curve which has $N_\mathrm{m}/N_\mathrm{f} = 1$. The beads belonging to the same MT as the bead in question were omitted for this calculation. The first peak occurs in the same point as the energy well indicated in Fig. S2. The beads which are at overlapping distances $(0.0 < r/r_\mathrm{min} < 0.5)$ occur near the confining wall due to the high attraction potential. The plot is normalised with the packing fraction of beads within the confinement.

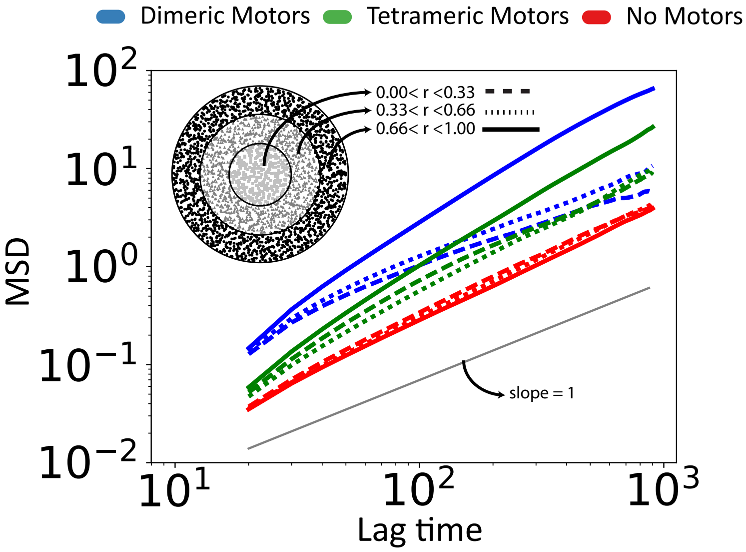

FIG. S22. Translational mean squared displacement (MSD) of MTs' center of masses by region. $E_\mathrm{A} = 0.2k_\mathrm{B}T$ and $N_\mathrm{m}/N_\mathrm{f} = 1$. The confinement is split into three sections, as illustrated in the inset. MTs whose centers of masses fall inside each of these sections at various time origins is used as a reference point to compute the MSD. If an MT leaves its original section, we continue to track it according to its position at the time origin. The region closest to the wall is the most dynamic in the cases with the tetrameric and dimeric motors. MSD is normalized using L^2. Lag time is normalised using the onset of the activity time scale, τ. The radial distance of the MT's center of mass, r is normalised by the radius of the confinement, R_W.

S.VI. SUPPLEMENTARY VIDEOS

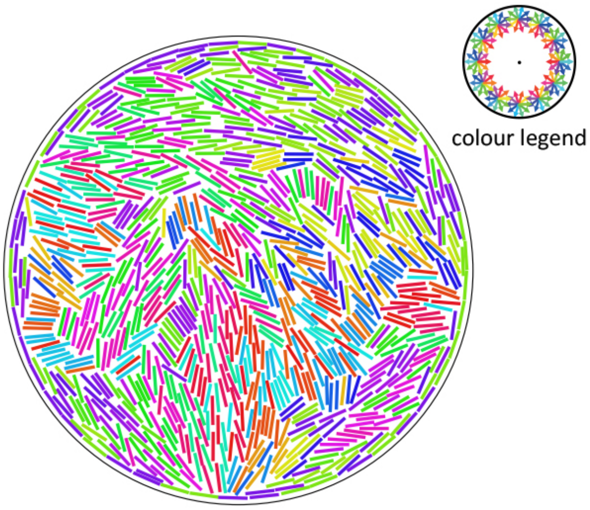

MOVIE S1. No motor system. Video shows the evolution of the system beginning from the random initial condition. The number on the top of the video is time in units of τ. Length units shown in the video are in terms of $r_{\min}$. $E_{\mathrm{A}} = 0.2k_{\mathrm{B}}T$ and $N_{\mathrm{m}}/N_{\mathrm{f}} = 0$.

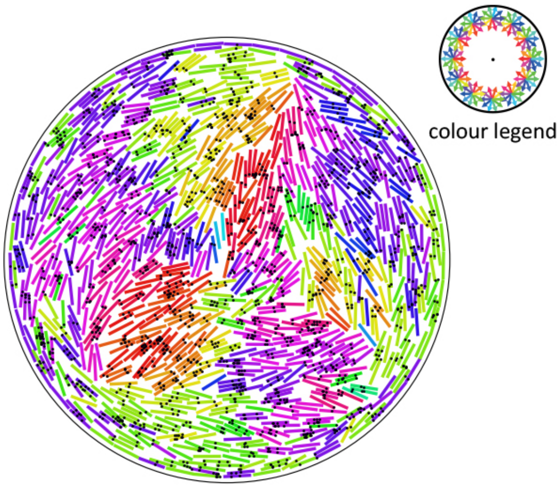

MOVIE S2. Dimeric motor system. Video shows the evolution of the dimeric motor system beginning from the random initial condition. The number on the top of the video is time in units of τ. Note the fast moving MTs at the edge of the confinement. Length units shown in the video are in terms of $r_{\min}$. $E_{\mathrm{A}} = 0.2k_{\mathrm{B}}T$ and $N_{\mathrm{m}}/N_{\mathrm{f}} = 1$.

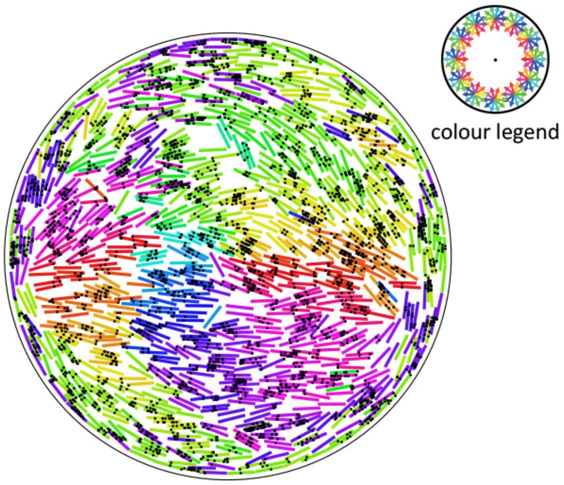

MOVIE S3. Dimeric motor system, at higher motor concentration. Video shows the evolution of the dimeric motor system beginning from the random initial condition. The number on the top of the video is time in units of τ. Note the fast moving MTs at the edge of the confinement. There are more spaces in between clusters since a higher concentration of motors binds MTs closer to each other. Length units shown in the video are in terms of r_{min}. $E_{\mathrm{A}} = 0.2 k_{\mathrm{B}} T$ and $N_{\mathrm{m}}/N_{\mathrm{f}} = 2$.

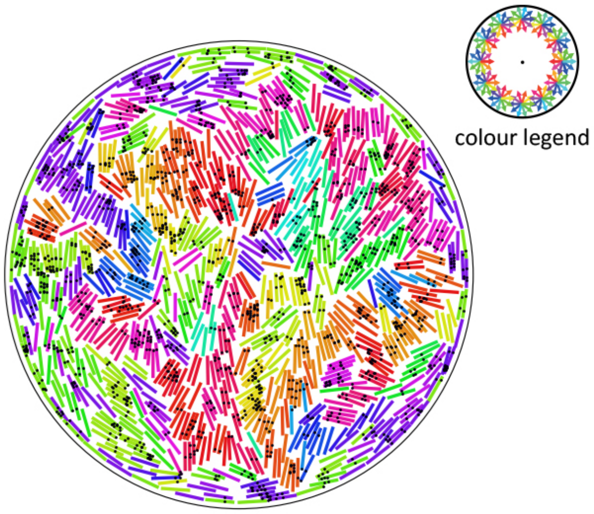

MOVIE S4. Tetrameric motor system. Video shows the evolution of the tetrameric motor system beginning from the random initial condition. The number on the top of the video is time in units of τ. Length units shown in the video are in terms of r_{min}. $E_{\mathrm{A}} = 0.2 k_{\mathrm{B}} T$ and $N_{\mathrm{m}}/N_{\mathrm{f}} = 1$.

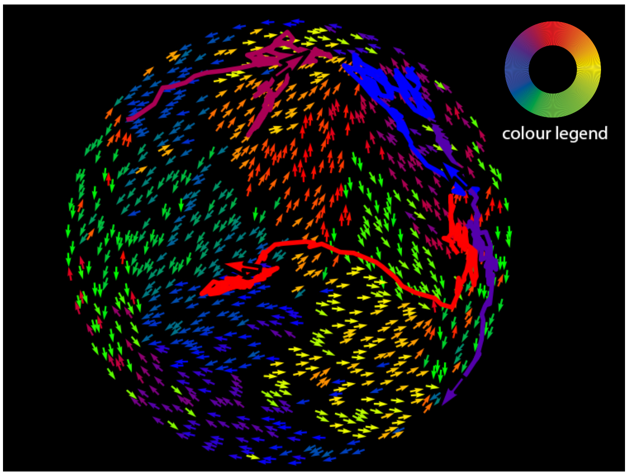

MOVIE S5. Dimeric motor system with trajectory of four probe MTs. The video corresponds to Fig. 8 in the main text. $E_\mathrm{A} = 0.2 k_\mathrm{B}T$ and $N_\mathrm{m}/N_\mathrm{f} = 1$.

SUPPORTING REFERENCES

[1] Howard, J., 2001. Mechanics of motor proteins and the cytoskeleton. Sinauer Associates Sunderland, Massachusetts.

[2] Hilitski, F., A. R. Ward, L. Cajamarca, M. F. Hagan, G. M. Grason, and Z. Dogic, 2015. Measuring Cohesion between Macromolecular Filaments One Pair at a Time: Depletion-Induced Microtubule Bundling. *Phys. Rev. Lett.* 114.

[3] Elgeti, J., and G. Gompper, 2013. Wall accumulation of self-propelled spheres. *EPL* 101:48003.

[4] Lu, W., M. Winding, M. Lakonishok, J. Wildonger, and V. I. Gelfand, 2016. Microtubule–microtubule sliding by kinesin-1 is essential for normal cytoplasmic streaming in Drosophila oocytes. *Proc. Natl. Acad. Sci. U.S.A.* 113:E4995–E5004.

[5] Löwen, H., 1994. Brownian dynamics of hard spherocylinders. *Phys. Rev. E* 50:1232–1243.

[6] Howard, J., A. J. Hudspeth, and R. D. Vale, 1989. Movement of microtubules by single kinesin molecules. *Nature* 342:154–158.

[7] Chrétien, D., and R. H. Wade, 1991. New data on the microtubule surface lattice. *Biol. Cell* 71:161–74.

[8] Wirtz, D., 2009. Particle-tracking microrheology of living cells: principles and applications. *Annu. Rev. Biophys* 38:301–26.

[9] Brady, S. T., K. K. Pfister, and G. S. Bloom, 1990. A monoclonal antibody against kinesin inhibits both anterograde and retrograde fast axonal transport in squid axoplasm. A monoclonal antibody against kinesin inhibits both anterograde and retrograde fast axonal transport in squid axoplasm. *Proc. Natl. Acad. Sci. U.S.A.* 87:1061–5.

[10] Schliwa, M., editor, 2003. Molecular Motors. Wiley-VCH, Weinheim.

[11] Crevel, I., N. Carter, M. Schliwa, and R. Cross, 1999. Coupled chemical and mechanical reaction steps in a processive Neurospora kinesin. *EMBO J* 18:5863–5872.

[12] Coppin, C. M., J. T. Finer, J. A. Spudich, and R. D. Vale, 1995. Measurement of the isometric force exerted by a single kinesin molecule. *Biophys. J.* 68:242S.

[13] Gao, T., R. Blackwell, M. A. Glaser, M. D. Betterton, and M. J. Shelley, 2015. Multiscale Polar Theory of Microtubule and Motor-Protein Assemblies. *Phys. Rev. Lett.* 114:048101.